Performance analysis of crosslink radiometric measurement based autonomous orbit determination for cislunar small satellite formations

Turan, Erdem; Speretta, Stefano; Gill, Eberhard

Important note
To cite this publication, please use the final published version (if applicable).
Please check the document version above.

Performance analysis of crosslink radiometric measurement based autonomous orbit determination for cislunar small satellite formations

Erdem Turan *, Stefano Speretta, Eberhard Gill

Delft University of Technology, Faculty of Aerospace Engineering, Kluyverweg 1, 2629 HS Delft, the Netherlands

Abstract

Recent advances in space technology provide an opportunity for small satellites to be launched in cislunar space. However, tracking these small satellites still depends on ground-based operations. Autonomous navigation could be a possible solution considering the challenges presented by costly ground operations and limited onboard power available for small satellites. There have been various studies on autonomous navigation methods for cislunar missions. One of them, LiAISON, provides an autonomous orbit determination solution solely using inter-satellite measurements. This study aims at providing a detailed performance analysis of crosslink radiometric measurements based on autonomous orbit determination for cislunar small satellite formations considering the effects of measurement type, measurement accuracy, bias, formation geometry, and network topology. This study shows that range observations provide better state estimation performance than range-rate observations for the autonomous navigation system in cislunar space. Line-of-sight angle measurements derived from radiometric measurements do not improve the overall system performance. In addition, less precise crosslink measurement methods could be an option for formations in highly observable orbital configurations. It was found that measurement biases and measurements with high intervals reduce the overall system performance. In case there are more than two spacecraft in the formation, the navigation system in the mesh topology provides a better overall state estimation than the centralized topology.
© 2022 COSPAR. Published by Elsevier B.V. This is an open access article under the CC BY license (http://creativecommons.org/licenses/by/4.0/).

Keywords: Navigation; Autonomy; Radiometric; Crosslink; Small satellite

1. Introduction

In recent years, there has been growing attention to small satellite missions to the Moon. A significant interest can be observed in cislunar space due to piggyback launch opportunities and the availability of data relay satellites in lunar orbits. The Artemis 1 mission, for example, provided an opportunity for exploring cislunar and deep space with ten CubeSats NASA (2015). These CubeSats have a variety of unique objectives on the way to the Moon. In addition

to the Artemis 1 mission, there are other small satellite missions led by various organizations such as ESA, (Speretta et al. (2022); Cervone et al. (2022); Rowe et al. (2021); Walker et al. (2018); Goldberg et al. (2019); Burgett et al. (2016); Thelen et al. (2017); Imken et al. (2016); Benedetto et al. (2019)) and various studies proposed in the literature (Mercer (2018); Mercer (2019); Bentum et al. (2018)). All those small satellite missions consider traditional ground-based navigation techniques, but this approach could be expensive, while the development of these missions is expected at a low cost. In addition, it is difficult to track all these small satellites due to the limited capacity of ground stations. Limitations also come from

---

* Corresponding author.
E-mail address: e.turan@tudelft.nl (E. Turan).

the satellites, such as onboard power available for communications. Considering all these challenges, an autonomous navigation system for cislunar missions could provide a possible solution.

There have been various studies on autonomous navigation methods for near-Earth missions (Rebordão (2013); Sheikh et al. (2006); Hill and Born (2008)). These methods are in general visual-based or based on crosslink radiometric measurements. This study focuses on the investigation of the crosslink radiometric navigation method which is a promising method for small satellites due to its simplicity and the use of existing technologies and systems. Cislunar space generally refers to the volume between Earth and the Moon including lunar orbits, orbits around the L1 point, near-rectilinear halo orbits, and others. However, L2 Halo orbits are also included in the analysis of this study. The crosslink radiometric navigation in cislunar space uses the Linked Autonomous Interplanetary Satellite Orbit Navigation (LiAISON) method which is an orbit determination method using solely satellite-to-satellite observations, such as range and/or range-rate, to estimate the absolute states of the involved spacecraft when at least one of the satellite orbits has a unique size, shape, and orientation A.Hill (2007). The characteristics of the acceleration function determine whether inter-satellite range or range-rate measurements can be used alone to estimate the absolute spacecraft states (position and velocity). In a symmetrical gravity field, there are no unique orbital configurations resulting from the acceleration function, which also has a symmetric time derivative, leading to no absolute position determination. However, cislunar missions could benefit from the asymmetric gravity or unique gravity field to build a dedicated positioning system.

The orbit determination performance of LiAISON depends on various factors, such as measurement type, accuracy, bias, frequency, relative geometry between satellites, and others. Regarding the measurement type, range-rate measurements provide better ground-based navigation solutions for deep space or cislunar missions than range measurements. However, for radio frequency-based crosslink autonomous navigation applications, a detailed analysis is required on which data types (range, range-rate, and Line-of-Sight (LOS) angles) provide superior navigation solutions. On the other hand, if the small satellite uses ranging for its navigation, the ranging signal reduces the power available for telemetry, which reduces the data rate that can be supported. For such cases, various ranging methods have been proposed in literature including time-derived and telemetry-based ranging methods (Andrews et al. (2010); Hamkins et al. (2015); Iraci and Gnam (2018)). However, these techniques don't provide accurate ranging solutions as using conventional methods and thus this would affect the orbit determination performance. This requires a realistic comparison between data types considering their expected performance to choose the best data type for the orbit determination process. In addition to those, other aspects may affect the navigation performance:

relative geometry between satellites and the number of satellites in the system. These points require a detailed investigation to understand the limits of crosslink radiometric navigation in the use of cislunar missions. This study aims at providing a realistic performance analysis. It also presents analytical calculations for the special case of autonomous spacecraft at cislunar orbits in particular by showing the results of observability, covariance, consider-covariance, and Monte Carlo analysis.

This paper is organized as follows: Section 2 shows the crosslink radiometric navigation method. In Section 3, corresponding radiometric measurements are presented. Orbit determination models and performance analysis tools are introduced in Section 4 and 5, respectively. Section 6 provides results and Section 7 presents the limitations of the study. Lastly, the conclusion is drawn in Section 8.

2. Crosslink radiometric navigation

In general, small satellites do not have sufficient onboard power for direct-to-Earth communication and data transmission in deep space or in cislunar space. Therefore, the mother spacecraft can be involved to support small satellites in such cases. This also allows using existing systems and technologies for navigation purposes. Basically, relative radiometric measurements, relative range/range-rate/angle, provide a relative navigation solution for the distributed satellite systems. Having absolute state information for the mothercraft is sufficient to derive the daughtercraft absolute states via the relative navigation solution. However, relative range measurements alone are not sufficient to determine the full states for Earth-orbiting satellites due to the rank defect problem Gao et al. (2014). Even using both range and range-rate measurements does not provide a full state estimation in the two-body problem Meng et al. (2010).

Autonomous navigation requires the estimation of the absolute position and velocity of a spacecraft without using any ground-based observation. In order to do that, spacecraft states must be observable from the available radiometric measurements between satellites (Fujimoto et al. (2012); Hill and Born (2007)). In other words, the size, shape, and orientation of the spacecraft orbit must be observable using the available radiometric measurements. Thus, the observability of the system depends on one of the spacecraft occupying a unique trajectory and this can be used as an absolute reference. In the symmetrical gravity field of the two-body problem such as Earth-orbiting satellites, there is no unique orbit due to the acceleration function and its symmetric derivative. Relative measurements, in a two-body problem, do not provide the absolute orientation of the orbital planes but only the relative orientation (Qin et al. (2019); A.Hill (2007)). The LiAISON method uses solely inter-satellite measurements to estimate absolute states when at least one of the spacecraft orbit has a unique size, shape, and orientation which can be found in cislunar space e.g. around libration points. Basically, grav-

itational perturbations of the Moon are sufficient for such unique orbital configurations to exist at the cislunar space and the Earth-Moon Lagrangian points. This method has been applied to mission studies at librations points, asteroids, and cislunar vicinity (A.Hill (2007); Hill and Born (2007); Leonard et al. (2012); Hesar et al. (2015); Wang et al. (2019); Hill et al. (2006); Hill and Born (2008); Turan et al. (2022a); Turan et al. (2022c); Leonard (2015); Thompson et al. (2022); Fujimoto et al. (2016)). The method will be applied in the CAPSTONE mission (Fig. 1) using a crosslink between Lunar Reconnaissance Orbiter (LRO) and the CAPSTONE CubeSat, (Cheetham (2021); Thompson et al. (2022)).

To achieve a better navigation accuracy via the LiAISON method, in general, non-coplanar orbital configurations and varying inter-satellite distances are required. More satellites are added to the constellation and having ground-based observations also increases the overall navigation accuracy. In this paper, these and other mission aspects will be studied with the help of performance analysis tools.

3. Crosslink radiometric data

Inter-satellite radiometric measurements can provide data for autonomous navigation: this section presents three main data types (range, range-rate, and LOS angles) derived from the radiometric measurements and presents how can they contribute to the autonomous navigation strategy.

3.1. Range

The inter-satellite distance can be measured either by the signal travel time from a transmitter (signal source) to a receiver or by the phase shift on a ranging signal at a receiver with respect to a transmitter. This process can either be one-way or two-way. However, one-way tracking requires very accurate time synchronization between the involved spacecraft. This is very hard to achieve in practice, espe-
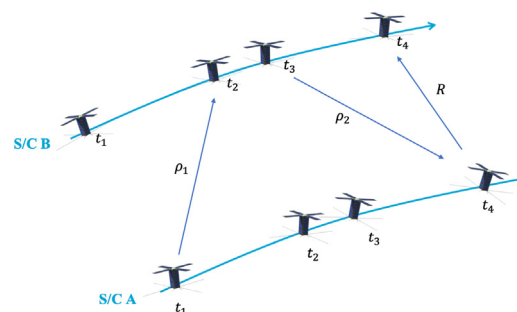

Fig. 2. Representation of the crosslink range measurement.

cially on small satellites with limited capabilities. That's why this option has not been considered in this study.

In a conventional two-way ranging using a ground station, an uplink ranging signal is received and retransmitted by the satellite. The downlink ranging signal is then received at the ground station to allow the computation of the two-way signal traveling time. The ranging signal can either be formed by sequential tones or a pseudonoise code, providing flexibility to the mission designers that can select the best-performing solution. The signal retransmission process can either be regenerative or transparent, depending on the amount of processing performed on-board the satellite. In regenerative ranging, the spacecraft demodulates and acquires the ranging code by correlation with a local replica from the uplink ranging signal and regenerates the ranging code on the downlink. This allows reducing the noise influence on the re-transmitted signal, lowering the required signal strength at the satellite receiver. In transparent ranging, the spacecraft translates the uplink ranging signal to the downlink without code acquisition CCSDS (2014). It would also be possible to use these techniques for inter-satellite ranging when the full logic could be implemented on a satellite.

Most commonly used radio-navigation transponders generate a downlink carrier that is phase-coherent to the uplink signal to maximize the navigation performance. However, small satellites often lack radio links with coher-
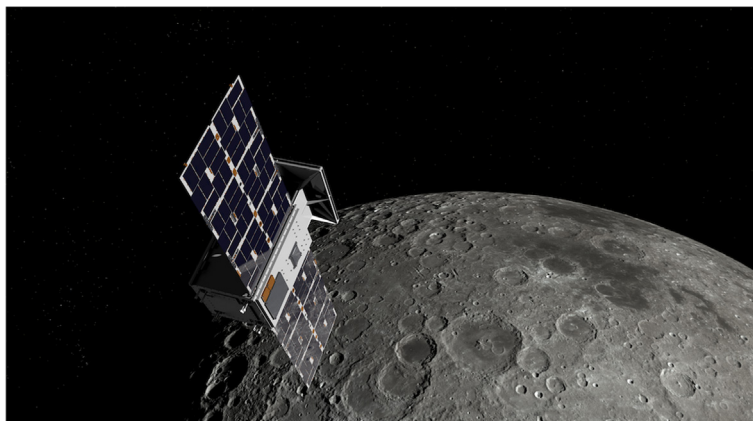

Fig. 1. CAPSTONE will perform crosslink radiometric navigation NASA (2020).

ent operations and thus use non-coherent pseudo-noise ranging which introduces a range bias in the measurements due to a chip rate mismatch between the replica and received codes CCSDS (2014) (besides also decreasing the range-rate estimation accuracy). In case of applying this method to a satellite formation in the cislunar space and considering a non-coherent transponder with a pseudo-noise square-wave shaped ranging signal, a chip tracking loop and an on-board loop bandwidth on the mothercraft wider than daughtercraft's, the following one-way ranging error would be observed CCSDS (2014):

$$\sigma_{\rho_{PN}} = \frac{c}{8 f_{rc}} \sqrt{\frac{B_L}{(P_{RC}/N_0)}} \qquad (1)$$

And the range bias due to a chip rate mismatch:

$$\rho_{\text{bias}} = \frac{c \Delta f_{chip} T}{4 f_{chip}} \qquad (2)$$

with c the speed of light, f_{rc} the frequency of the ranging clock component, B_L one-sided loop noise bandwidth, P_{RC} power of the ranging clock component, T integration time, N_0 one-side noise power spectral density, Δf_{chip} the difference in frequency between the received chip rate and the local chip rate.

However, using conventional ranging methods would require a certain amount of onboard power for the down-link ranging signal. This results in limited power availability for the telemetry signal. This issue could be solved by performing telemetry-based ranging which provides a round-trip light time solution derived from the telemetry stream (Hamkins et al. (2015); Andrews et al. (2010)). Telemetry-based ranging does not require any downlink ranging signal but it provides the delay between the acquired uplink ranging signal and the start of the next telemetry stream. Basically, all timing data are collected by the signal source to calculate a round-trip light time solution which includes the two-way light time propagation and the re-transmission delay. One of the major advantages of this method is having ranging and telemetry transmission at the same time, removing the need to perform separate tracking sessions or multiplexing tracking and telemetry sessions. Secondly, this method is based on the data rate and even low data rates would provide a ranging solution as good as conventional tone or pseudo-noise ranging. Considering a direct-to-Earth link, telemetry-based ranging provides better than conventional pseudo-noise ranging measurements at a data rate of about 15 kbps while using a correlator method Andrews et al. (2010). Considering a square wave uplink range clock and BPSK-modulated data, the performance of the telemetry-based ranging can be given as Andrews et al. (2010):

$$\sigma_{\rho_{TM}} = \left(1 - \frac{2v}{c}\right) \left(\frac{4 c T_{sd}^2}{\pi T_l E_S/N_0} + \frac{c}{8 f_{rc}} \sqrt{\frac{B_L}{(P_{RC}/N_0)}}\right) \qquad (3)$$

with T_{sd} the channel symbol duration, T_l the correlator integration time and E_S/N_0 the code symbol-to-noise ratio.

In the telemetry-based ranging, the uplink ranging signal is yet required and the traditional ground uplink signals could be used Hamkins et al. (2015) but any type of uplink signal could be used as well: a more power-efficient solution could be selected, for example, for a small satellite implementing a cross-link.

Another way to compute the round-trip light time between satellites is based on time transfer, as in the CCSDS Proximity-1 Space Link Protocol CCSDS (2013), where time correction, correlation, and distribution are standard services. Users can exchange epochs between satellites and derive the round-trip light time. This process requires obtaining four successive timestamps (time of transmission and reception of both spacecraft) and calculating the round trip light time and offset Woo et al. (2010).

In Iraci and Gnam (2018), a very similar method was proposed, where the round-trip light time has been measured from ping requests directly using the satellite radio. From the hardware testing, a ranging precision has been found as 155m (1σ) under strong signal conditions and 303m (1σ) under realistic worst-case conditions for 10kbps data rate. Strong signal conditions refer to a Bit Error Rate (BER) 10^{-5} or lower while worst-case conditions refer to a BER of 10^{-4}. Basically, this method does not provide a precise ranging solution, but this can still be sufficient to meet navigation requirements for certain missions. If timing is measured in units of telemetry/telecommand symbols, instead of directly in seconds, the downlink equation given in Eq. (3) of the telemetry-based ranging could be used for both links. Based on the same assumptions used in Eq. (3), and assuming T_l, E_S/N_0 are the same on both downlink and uplink sides, the performance of the time-derived ranging is:

$$\sigma_{\rho_{TD}} = \left(1 - \frac{2v}{c}\right) \left(\frac{4 c \sqrt{T_{sd\,U}^4 + T_{sd\,D}^4}}{\pi T_l E_S/N_0}\right) \qquad (4)$$

with $T_{sd\,U}$ and $T_{sd\,D}$ the symbol duration for uplink and downlink respectively.
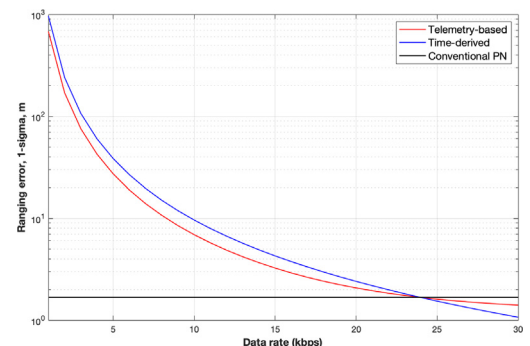

Fig. 3. Performance comparison of the ranging methods.

A comparison of all these three ranging methods is shown in Fig. 3. As it can be seen, the conventional pseudo-noise ranging is not a function of data rate (but of the navigation signal chip rate, independent of the data transmission rate). On the other hand, the telemetry-based ranging and the time-derived ranging methods show improved performances with increased data rates.

3.2. Range-rate

A basic physical phenomenon, the Doppler effect, is used to measure the relative range rate. Basically, the Doppler-shifted transmitted signal frequency arriving at the receiver provides an estimation of the relative velocity. It is also possible to derive range-rate from successive range measurements but all these techniques suffer from measurement errors.

This observation type is also affected by both random (instrumental and propagation noise) and systematic errors Asmar et al. (2005). However, the most dominant error for Doppler measurement is thermal noise. Measurement error for two-way Doppler due to thermal noise can be approximated by DSN (2018):

$$\sigma_V = \frac{c}{2\sqrt{2}\pi f_c T} \sqrt{\frac{1}{\rho_L} + \frac{G^2 B_L}{(P_C/N_0)}} \qquad (5)$$

where f_c the downlink carrier frequency, P_C/N_0 uplink carrier power to noise spectral density ratio, ρ_L the downlink carrier loop signal-to-noise ratio, G the turn-around ratio. In one of the Europa Clipper piggyback mission proposals, the Europa Tomography Probe (ETP) Benedetto et al. (2019) two-way coherent X-band Doppler data from the Inter-Satellite Link (ISL) between Europa Clipper and ETP will be used for orbit determination (with an expected range rate error of 0.012mm/s with an integration time τ of 60s).

3.3. Line-of-Sight direction

The full LOS direction can be calculated via the time delay or phase shift of the incoming signal with at least three antennas, in order to calculate two angles, mounted on a baseline at a certain distance, b, Fehse (2003). Fig. 4 shows the principle of LOS measurement via two antennas. On small satellites, due to size constraints, the antenna
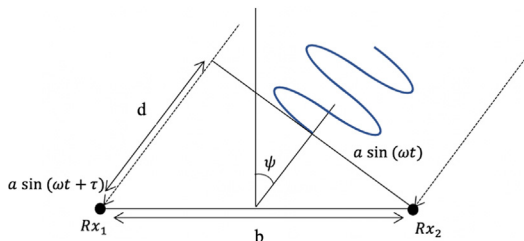
baseline is often shorter than the wavelength, simplifying the calculations as wavelength ambiguity is eliminated. The following equations can be used to estimate the angle ψ between the line toward the signal source and the line perpendicular to the baseline, b, via the time delay Δt:

$$\Delta t = \frac{b}{c} \cos \psi \qquad (6)$$

or via the phase-shift,

$$\tau = \frac{2\pi b}{\lambda} \sin \psi \qquad (7)$$

Basically, the LOS measurement accuracy depends on the length of the baseline and time-delay/phase-shift measurement accuracy (ranging accuracy). Taking the variance of both hand sides of the above equations would give the relation between range measurement accuracy σ_ρ and the LOS measurement accuracy σ_ψ, via the time delay (See Appendix A for the full derivation):

$$\sigma_\rho = b\sqrt{\frac{1 - e^{-2\sigma_\psi^2}}{2}} \qquad (8)$$

or via the phase-shift:

$$\sigma_\tau = \frac{2\pi b}{\lambda} \sqrt{\frac{1 - e^{-2\sigma_\psi^2}}{2}} \qquad (9)$$

The relation between LOS and the range measurement error can be seen in Fig. 5 for a baseline of 1m.

4. Orbit determination models

In this section, orbit determination models used in this study are presented. Dynamical model, observation models, and estimation models are shown in the following subsections.

4.1. Orbit dynamics model

This section presents the orbital dynamics model used in this paper. Dynamic models are formulated based on the Circular Restricted Three-body Problem (CRTBP). This model is simple but accurate enough for many applica-

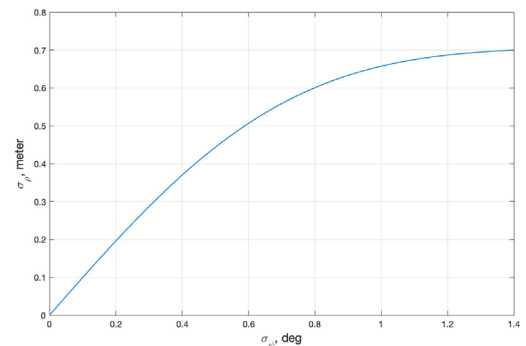Fig. 4. LOS measurement via two-antennas.

Fig. 5. Relation between LOS angle and range measurement errors.

tions: in A.Hill (2007), the autonomous orbit determination accuracy remained at the same order of magnitude for various force models (CRTBP and JPL DE405 Ephemeris). Therefore, the CRTBP is selected for analysis in this study. The CRTBP assumes that there are two massive bodies, Earth (P_1) and Moon (P_2) in this case with masses m_1 and m_2 respectively, moving under their mutual gravitation in a circular orbit around each other with a radius r_{12}, Curtis (2020). Considering a non-inertial, co-moving reference frame (Fig. 6) with its origin at the barycenter of the two bodies, the x–direction pointing from barycenter to P_2. The positive y–axis is parallel to the velocity vector of P_2 and the z–axis is perpendicular to the orbital plane.

Considering a third body of mass m_3 with $m_3 \ll m_1$ and $m_3 \ll m_2$, it cannot impact the motion of primary bodies, P_1 and P_2. Using Newton's second law, the equations describing the motion of the third body P_3

$$m_3\ddot{\mathbf{r}} = -\frac{Gm_1m_3}{r_1^3}\mathbf{r}_1 - \frac{Gm_2m_3}{r_2^3}\mathbf{r}_2 \tag{10}$$

where G is the universal gravitational constant. Note that the absolute acceleration of m_3 requires differentiation in the inertial frame Daniel (2006). By using the characteristic quantities

$$l^* = r_{12}, t^* = \sqrt{l^{*3}/G(m_1 + m_2)} \tag{11}$$

Eq. (10) can be non-dimensionalize as

$$\frac{d^2\mathbf{r}}{d\tau^2} = -\frac{\mu}{r_1^3}\mathbf{r}_1 - \frac{1-\mu}{r_2^3}\mathbf{r}_2 \tag{12}$$

where $\mu = m_2/(m_1 + m_2)$ and the non-dimensional time $\tau = t/t^*$. Note that the position vectors, $\mathbf{r}, \mathbf{r}_1$ and $\mathbf{r}_2$, are now non-dimensional (e.g., $\mathbf{r}_{non-dim} = \mathbf{r}_{dim}/l^*$). The angular velocity of the rotating frame with respect to the inertial frame is written $\mathbf{\Omega} = n\hat{z}$ where the non-dimensional mean motion is $n = 1$, Daniel (2006). After the differentiation of $\mathbf{r}$ twice with respect to an inertial observer, the equations of motion for the CRTBP Daniel (2006) are
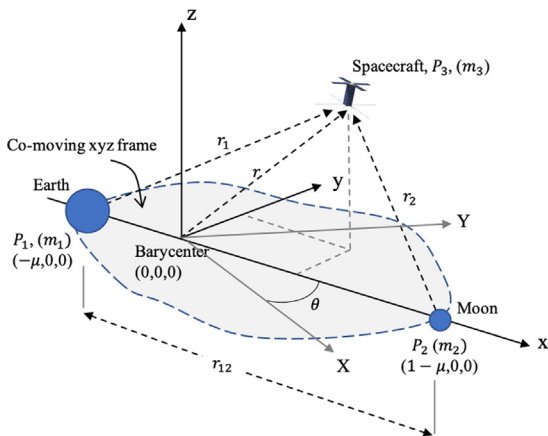
$$\ddot{x} - 2\dot{y} = x - (1-\mu)\frac{x+\mu}{r_1^3} - \mu\frac{x+\mu-1}{r_2^3} \tag{13}$$

$$\ddot{y} + 2\dot{x} = \left(1 - \frac{1-\mu}{r_1^3} - \frac{\mu}{r_2^3}\right)y \tag{14}$$

$$\ddot{z} = \left(\frac{\mu-1}{r_1^3} - \frac{\mu}{r_2^3}\right)z \tag{15}$$

where $r_1 = \sqrt{(x+\mu)^2 + y^2 + z^2}$ and $r_2 = \sqrt{(x+\mu-1)^2 + y^2 + z^2}$. For the Earth-Moon system, $\mu = 0.01215, t^* = 4.343$, and $l^* = 384747.96$, respectively.

4.2. Observation models

Considering a formation formed by two spacecraft, the estimated state vector with position and velocity components of both spacecraft is

$$\mathbf{X} = \begin{bmatrix} x_1 & y_1 & z_1 & \dot{x}_1 & \dot{y}_1 & \dot{z}_1 & x_2 & y_2 & z_2 & \dot{x}_2 & \dot{y}_2 & \dot{z}_2 \end{bmatrix}^T \tag{16}$$

Measuring the round-trip light time, in general, is based on phase measurement of a ranging signal and, in this way, the on-board clock will be used as a time reference, potentially causing a measurement bias. This bias is either measured along with the navigation filter or calibrated. The measurement model in this paper, referred to as the pseudorange, involves the geometric range, the overall clock bias, and other error sources. In Figs. 2 and 7, the concept of the two-way ranging measurement can be seen. Basically, spacecraft A transmits a ranging signal at time t_1 to spacecraft B (who receives it at time t_2 and re-transmits it at time t_3) and receives it back at time t_4. During this measurement interval, both spacecraft are moving in their orbits, so there are also changes in line-of-sight direction which can be modeled as $\Delta\rho$. In the end, we can model the geometric range as:

$$R = \frac{1}{2}c(t_4 - t_1) + \Delta\rho \tag{17}$$

By assuming the speed of light is greater than the spacecraft's relative velocity, $c \gg v$, and ignoring the light-time correction, the geometric range can be modeled as:

$$R = \sqrt{(x_1 - x_2)^2 + (y_1 - y_2)^2 + (z_1 - z_2)^2} \tag{18}$$

Fig. 6. Formulation of the Circular Restricted Three-Body Problem: a rotating, non-dimensional coordinate frame.
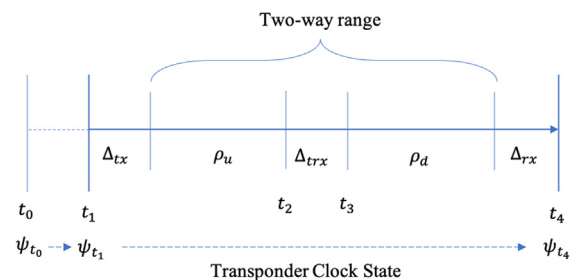

Fig. 7. Two-way round-trip light time measurement.

Then the pseudorange observations can be modeled as:

$$\rho = R + c(\psi_{t_3} - \psi_{t_1}) + c(\Delta_{tx} + \Delta_{rx}) + c\Delta_{trx} + \rho_{\text{noise}}$$

$$\rho = \sqrt{(\mathbf{r}_1 - \mathbf{r}_2) \cdot (\mathbf{r}_1 - \mathbf{r}_2)} + \rho_{\text{bias}} + \rho_{\text{noise}} \tag{19}$$

where ψ_{t_4} and ψ_{t_1} are the clock states at t_4 and t_1, respectively. The transponder transmit and receive line delays are Δ_{tx} and Δ_{rx}, respectively, and Δ_{trx} is the line delay on the spacecraft transponding the ranging signal. All these terms are combined as ρ_{bias} and ρ_{noise} representing the unmodelled statistical error sources.

The range rate measurements, $\dot{\rho}$, can be modeled as:

$$\dot{\rho} = \frac{\boldsymbol{\rho} \cdot \dot{\boldsymbol{\rho}}}{\rho} \tag{20}$$

$$\dot{\rho} = \frac{(x_1 - x_2)(\dot{x}_1 - \dot{x}_2) + (y_1 - y_2)(\dot{y}_1 - \dot{y}_2) + (z_1 - z_2)(\dot{z}_1 - \dot{z}_2)}{\sqrt{(x_1 - x_2)^2 + (y_1 - y_2)^2 + (z_1 - z_2)^2}}$$

$$+ \dot{\rho}_{\text{bias}} + \dot{\rho}_{\text{noise}} \tag{21}$$

Finally, the LOS angle measurements can be modeled as:

$$\phi = \arctan\left(\frac{y_2 - y_1}{x_2 - x_1}\right) + \phi_{\text{bias}} + \phi_{\text{noise}} \tag{22}$$

$$\varphi = \arcsin\left(\frac{z_2 - z_1}{\sqrt{(x_1 - x_2)^2 + (y_1 - y_2)^2 + (z_1 - z_2)^2}}\right)$$

$$+ \varphi_{\text{bias}} + \varphi_{\text{noise}} \tag{23}$$

where ϕ is a relative azimuth angle, φ is a relative elevation angle between the two spacecraft.

4.3. Estimation model

This study uses an Extended Kalman Filter (EKF) for real-time navigation. The EKF consists of two steps: prediction and correction. In the prediction step, predicted state and error covariance prediction $\overline{P}$ are Tapley et al. (2004)

$$\dot{\mathbf{X}} = \boldsymbol{F}(\mathbf{X}, t), \mathbf{X}(t_{k-1}) = \hat{\mathbf{X}}_{k-1} \tag{24}$$

$$\overline{\boldsymbol{P}}_k = \boldsymbol{\Phi}(t_k, t_{k-1})\boldsymbol{P}_{k-1}\boldsymbol{\Phi}^T(t_k, t_{k-1}) + \boldsymbol{Q} \tag{25}$$

where $\boldsymbol{\Phi}(t_k, t_{k-1})$ is state transition matrix from t_{k-1} to t_k and $\boldsymbol{Q}$ is the process noise matrix. The correction step:

$$\boldsymbol{K}_k = \overline{\boldsymbol{P}}_k \widetilde{\boldsymbol{H}}_k^T \left[\widetilde{\boldsymbol{H}}_k \overline{\boldsymbol{P}}_k \widetilde{\boldsymbol{H}}_k^T + \boldsymbol{W}_k\right]^{-1} \tag{26}$$

$$\hat{\mathbf{X}}_k = \mathbf{X}_k + \boldsymbol{K}_k \left[\mathbf{y}_k - \widetilde{\boldsymbol{H}}_k \mathbf{X}_k\right] \tag{27}$$

$$\boldsymbol{P}_k = \left[\boldsymbol{I} - \boldsymbol{K}_k \widetilde{\boldsymbol{H}}_k\right] \overline{\boldsymbol{P}}_k \tag{28}$$

where $\widehat{X}$ is the state estimate, $\boldsymbol{K}$ is the Kalman gain, $\widetilde{H}$ is the measurement sensitivity, $\boldsymbol{P}$ is the estimated error covariance matrix, and $\boldsymbol{W}$ is the measurement noise compensation matrix. In this study, it is assumed that the

observation errors are modeled as white Gaussian noise with standard deviation σ_ρ and the measurement noise covariance matrix, $\boldsymbol{W}$, is formed as $W = \sigma_\rho^2$ for the range-only scenario. The process noise covariance matrix is built based on the following equations:

$$\boldsymbol{Q} = \begin{bmatrix} \boldsymbol{Q}_1 & 0_{6\times6} \\ 0_{6\times6} & \boldsymbol{Q}_2 \end{bmatrix}, \boldsymbol{Q}_m = \begin{bmatrix} \frac{\Delta t^4 \sigma_i^2}{3}\mathbf{I}_{3\times3} & \frac{\Delta t^3 \sigma_i^2}{2}\mathbf{I}_{3\times3} \\ \frac{\Delta t^3 \sigma_i^2}{2}\mathbf{I}_{3\times3} & \Delta t^2 \sigma_i^2 \mathbf{I}_{3\times3} \end{bmatrix}, m = 1, 2 \tag{29}$$

where Δt is a time interval between measurements and σ_i is the standard deviation of unknown acceleration which has been tuned until finding a realistic error covariance matrix by trial and error.

5. Performance analysis

Throughout this study, several performance analysis methods were applied, including the observability analysis, the covariance analysis, and the Monte Carlo analysis. This section begins with the basic concept of observability presenting its definition and the observability criteria for crosslink radiometric measurement-based autonomous navigation, mainly introducing the observability analysis methods. As part of the observability analysis, Singular Value Decomposition (SVD), observability Gramian, and estimation error covariance were considered. Next, the Monte Carlo analysis is discussed. Lastly, an observation type comparison is provided for the autonomous navigation system, showing which observable (range, range-rate, and LOS) would provide a better navigation solution.

5.1. Observability analysis

The observability analysis of an autonomous navigation system allows investigating the relationship between navigation performance and measurement type, frequency, precision, and accuracy. This analysis also allows investigating the relation between the estimation accuracy and other aspects such as inter-satellite distance, orbital periods, and the number of spacecraft in the formation. Basically, the observability analysis may help testing whether the navigation parameters could be determined by observation data. However, it does not directly give insight into the estimation accuracy. In fact, the degree of observability can be used alone to evaluate the estimation accuracy. If the degree of observability or in other words state observability is increased, this means an increased reduction of estimated state uncertainty Dianetti et al. (2017). The standard approach to measure observability is checking the observability rank condition which, unfortunately, only provides information on whether the system is observable or not. The degree of observability can be either evaluated via the observability Gramian or the information matrix. Both methods are related to each other via the measurement covariance matrix which provides weighted information

about its observability. One of the possible observability assessments would be the use of SVD of either the observability Gramian or the information matrix. This provides the observability of the modes of the system allowing to find higher and lower observable states. It is also possible to evaluate the degree of observability via the condition number, which is the ratio of the largest singular value to the smallest one. Another possible measure is the local unobservability index which is the reciprocal of the smallest local singular value. If it is large, then observation noise would have a large impact on the estimation error Krener and Ide (2009). The local unobservability index will not increase with additional observations but the condition number might increase. In brief, a higher degree of observability indicates, in general, a more accurate estimation.

Under a discrete time assumption, the time-varying observability Gramian can be written as:

$$N = \sum_{k=1}^{l} \mathbf{\Phi}(t_k, t_0)^T \widetilde{\boldsymbol{H}}_k^T \widetilde{\boldsymbol{H}}_k \mathbf{\Phi}(t_k, t_0) \tag{30}$$

Theoretical analysis can be conducted based on the observability Gramian to show the observable states or state combinations. If the Gramian has a full rank, which means all columns are linearly independent from each other, the whole system is observable and all states can be estimated by a navigation filter. If there are linearly dependent columns, the corresponding states are unobservable. If there exists a linear combination of the dependent columns, which is independent from other columns, the corresponding linear state combination is observable, and the total amount of observable states and state combinations is equal to the rank of the observability matrix.

Another observability approach would be based on the information matrix given as:

$$\mathbf{\Lambda} = \boldsymbol{H}^T \boldsymbol{W} \boldsymbol{H} = \sum_{k=1}^{l} \boldsymbol{H}_k^T \boldsymbol{W} \boldsymbol{H}_k \tag{31}$$

The information matrix is similar to the observability Gramian with the addition of a measurement noise covariance matrix, $\boldsymbol{W}$. The condition number $cond(\mathbf{\Lambda})$ or $cond(\boldsymbol{N})$, which is the ratio of the largest singular value to the smallest one, provides an indication of the observability. Using the information matrix in Eq. 31, the SVD can be performed as:

$$\mathbf{\Lambda} = \boldsymbol{U} \mathbf{\Sigma} \boldsymbol{V}^T \tag{32}$$

where $\boldsymbol{U}$ and $\boldsymbol{V}$ are unitary matrices and $\mathbf{\Sigma}$ is a matrix of singular values. It is also possible to evaluate the degree of observability by investigating the singular values in a matrix Yim et al. (2000). The state with the largest singular value is the most observable one and it gives the most observable information. Similarly, the state with the smallest singular value is the least observable in the system. By

using $\boldsymbol{V}^T$, states corresponding to each singular value can be found: the largest number in the columns of $\boldsymbol{V}^T$ corresponding to any singular value shows the related states. By looking at all the columns of $\boldsymbol{V}^T$, we can sort the states from the most observable one to the least observable one. In addition to the previous points, it is also possible to check the effectiveness of the observation at t_i alone on the position/velocity of a specific spacecraft. This can be done by taking the square root of the maximum eigenvalue of each $\mathbf{\Lambda}_k$ or 3×3 position/velocity component of $\mathbf{\Lambda}_i$, $\left(\sqrt{\max \text{eig}\left(\mathbf{\Lambda}_{i(3\times3)}\right)} \right)$ A.Hill (2007). Both observability analysis methods require $\boldsymbol{H}$ and thus $\widetilde{\boldsymbol{H}}$ and $\mathbf{\Phi}(t_k, t_0)$ to be calculated.

The observations can be related to the states with a partial differential matrix at time t_k. In the case of crosslink range measurements, ρ is the observation type then $\widetilde{\boldsymbol{H}}$ is of the form:

$$\widetilde{\boldsymbol{H}}_k^\rho = \begin{bmatrix} \frac{\partial \rho}{\partial x_1} & \frac{\partial \rho}{\partial y_1} & \frac{\partial \rho}{\partial z_1} & \frac{\partial \rho}{\partial \dot{x}_1} & \frac{\partial \rho}{\partial \dot{y}_1} & \frac{\partial \rho}{\partial \dot{z}_1} & \frac{\partial \rho}{\partial x_2} & \frac{\partial \rho}{\partial y_2} & \frac{\partial \rho}{\partial z_2} & \frac{\partial \rho}{\partial \dot{x}_2} & \frac{\partial \rho}{\partial \dot{y}_2} & \frac{\partial \rho}{\partial \dot{z}_2} \end{bmatrix} \tag{33}$$

$$\widetilde{\boldsymbol{H}}_k^\rho = \begin{bmatrix} \frac{(x_1-x_2)}{\rho} & \frac{(y_1-y_2)}{\rho} & \frac{(z_1-z_2)}{\rho} & 0 & 0 & 0 & \frac{-(x_1-x_2)}{\rho} & \frac{-(y_1-y_2)}{\rho} & \frac{-(z_1-z_2)}{\rho} & 0 & 0 & 0 \end{bmatrix} \tag{34}$$

In case of range-rate, $\dot{\rho}$, is the observation type then $\widetilde{\boldsymbol{H}}$ is of the form:

$$\widetilde{\boldsymbol{H}}_k^{\dot{\rho}} = \begin{bmatrix} \frac{\partial \dot{\rho}}{\partial x_1} & \frac{\partial \dot{\rho}}{\partial y_1} & \frac{\partial \dot{\rho}}{\partial z_1} & \frac{\partial \dot{\rho}}{\partial \dot{x}_1} & \frac{\partial \dot{\rho}}{\partial \dot{y}_1} & \frac{\partial \dot{\rho}}{\partial \dot{z}_1} & \frac{\partial \dot{\rho}}{\partial x_2} & \frac{\partial \dot{\rho}}{\partial y_2} & \frac{\partial \dot{\rho}}{\partial z_2} & \frac{\partial \dot{\rho}}{\partial \dot{x}_2} & \frac{\partial \dot{\rho}}{\partial \dot{y}_2} & \frac{\partial \dot{\rho}}{\partial \dot{z}_2} \end{bmatrix} \tag{35}$$

$$\widetilde{\boldsymbol{H}}_k^{\dot{\rho}} = \begin{bmatrix} \frac{(\dot{x}_1-\dot{x}_2)}{\rho} - \frac{(x_1-x_2)((x_1-x_2)(\dot{x}_1-\dot{x}_2)+ (y_1-y_2)(\dot{y}_1-\dot{y}_2)+(z_1-z_2)(\dot{z}_1-\dot{z}_2))}{\rho^3} \\ \frac{(\dot{y}_1-\dot{y}_2)}{\rho} - \frac{(y_1-y_2)((x_1-x_2)(\dot{x}_1-\dot{x}_2)+ (y_1-y_2)(\dot{y}_1-\dot{y}_2)+(z_1-z_2)(\dot{z}_1-\dot{z}_2))}{\rho^3} \\ \frac{(\dot{z}_1-\dot{z}_2)}{\rho} - \frac{(z_1-z_2)((x_1-x_2)(\dot{x}_1-\dot{x}_2)+ (y_1-y_2)(\dot{y}_1-\dot{y}_2)+(z_1-z_2)(\dot{z}_1-\dot{z}_2))}{\rho^3} \\ \frac{(x_1-x_2)}{\rho} \\ \frac{(y_1-y_2)}{\rho} \\ \frac{(z_1-z_2)}{\rho} \\ -\frac{(\dot{x}_1-\dot{x}_2)}{\rho} + \frac{(x_1-x_2)((x_1-x_2)(\dot{x}_1-\dot{x}_2)+ (y_1-y_2)(\dot{y}_1-\dot{y}_2)+(z_1-z_2)(\dot{z}_1-\dot{z}_2))}{\rho^3} \\ -\frac{(\dot{y}_1-\dot{y}_2)}{\rho} + \frac{(y_1-y_2)((x_1-x_2)(\dot{x}_1-\dot{x}_2)+ (y_1-y_2)(\dot{y}_1-\dot{y}_2)+(z_1-z_2)(\dot{z}_1-\dot{z}_2))}{\rho^3} \\ -\frac{(\dot{z}_1-\dot{z}_2)}{\rho} + \frac{(z_1-z_2)((x_1-x_2)(\dot{x}_1-\dot{x}_2)+ (y_1-y_2)(\dot{y}_1-\dot{y}_2)+(z_1-z_2)(\dot{z}_1-\dot{z}_2))}{\rho^3} \\ -\frac{(x_1-x_2)}{\rho} \\ -\frac{(y_1-y_2)}{\rho} \\ -\frac{(z_1-z_2)}{\rho} \end{bmatrix}^T \tag{36}$$

If LOS angles, ϕ and φ, are selected observation types, then $\widetilde{\boldsymbol{H}}$ is of the form:

$$\widetilde{\boldsymbol{H}}_k^\phi = \begin{bmatrix} \frac{\partial \phi}{\partial x_1} & \frac{\partial \phi}{\partial y_1} & \frac{\partial \phi}{\partial z_1} & \frac{\partial \phi}{\partial \dot{x}_1} & \frac{\partial \phi}{\partial \dot{y}_1} & \frac{\partial \phi}{\partial \dot{z}_1} & \frac{\partial \phi}{\partial x_2} & \frac{\partial \phi}{\partial y_2} & \frac{\partial \phi}{\partial z_2} & \frac{\partial \phi}{\partial \dot{x}_2} & \frac{\partial \phi}{\partial \dot{y}_2} & \frac{\partial \phi}{\partial \dot{z}_2} \end{bmatrix} \tag{37}$$

$$\widetilde{\boldsymbol{H}}_k^\phi = \left[\frac{-(y_1-y_2)}{(x_1-x_2)^2\left(\left(\frac{(y_1-y_2)^2}{(x_1-x_2)^2}\right)+1\right)} \quad \frac{1}{(x_1-x_2)\left(\frac{(y_1-y_2)^2}{(x_1-x_2)^2}+1\right)} \quad 0 \quad 0 \quad 0 \quad 0 \quad \frac{(y_1-y_2)}{(x_1-x_2)^2\left(\left(\frac{(y_1-y_2)^2}{(x_1-x_2)^2}\right)+1\right)} \quad \frac{-1}{(x_1-x_2)\left(\frac{(y_1-y_2)^2}{(x_1-x_2)^2}+1\right)} \quad 0 \quad 0 \quad 0 \quad 0\right] \tag{38}$$

$$\widetilde{\boldsymbol{H}}_k^\varphi = \left[\frac{\partial\varphi}{\partial x_1} \quad \frac{\partial\varphi}{\partial y_1} \quad \frac{\partial\varphi}{\partial z_1} \quad \frac{\partial\varphi}{\partial \dot{x}_1} \quad \frac{\partial\varphi}{\partial \dot{y}_1} \quad \frac{\partial\varphi}{\partial \dot{z}_1} \quad \frac{\partial\varphi}{\partial x_2} \quad \frac{\partial\varphi}{\partial y_2} \quad \frac{\partial\varphi}{\partial z_2} \quad \frac{\partial\varphi}{\partial \dot{x}_2} \quad \frac{\partial\varphi}{\partial \dot{y}_2} \quad \frac{\partial\varphi}{\partial \dot{z}_2}\right] \tag{39}$$

$$\widetilde{\boldsymbol{H}}_k^\varphi = \begin{bmatrix} \frac{(2x_1-2x_2)(z_1-z_2)}{\left(2\left(1-(z_1-z_2)^2/((x_1-x_2)^2+(y_1-y_2)^2+(z_1-z_2)^2)\right)\right)^{1/2}\left((x_1-x_2)^2+(y_1-y_2)^2+(z_1-z_2)^2\right)^{3/2}} \\ \frac{(2y_1-2y_2)(z_1-z_2)}{\left(2\left(1-(z_1-z_2)^2/((x_1-x_2)^2+(y_1-y_2)^2+(z_1-z_2)^2)\right)\right)^{1/2}\left((x_1-x_2)^2+(y_1-y_2)^2+(z_1-z_2)^2\right)^{3/2}} \\ \frac{-(x_1^2-2x_1x_2+x_2^2+y_1^2-2y_1y_2+y_2^2)}{\left(1-(z_1-z_2)^2/((x_1-x_2)^2+(y_1-y_2)^2+(z_1-z_2)^2)\right)^{1/2}\left((x_1-x_2)^2+(y_1-y_2)^2+(z_1-z_2)^2\right)^{3/2}} \\ 0 \\ 0 \\ 0 \\ \frac{-(2x_1-2x_2)(z_1-z_2)}{\left(2\left(1-(z_1-z_2)^2/((x_1-x_2)^2+(y_1-y_2)^2+(z_1-z_2)^2)\right)\right)^{1/2}\left((x_1-x_2)^2+(y_1-y_2)^2+(z_1-z_2)^2\right)^{3/2}} \\ \frac{-(2y_1-2y_2)(z_1-z_2)}{\left(2\left(1-(z_1-z_2)^2/((x_1-x_2)^2+(y_1-y_2)^2+(z_1-z_2)^2)\right)\right)^{1/2}\left((x_1-x_2)^2+(y_1-y_2)^2+(z_1-z_2)^2\right)^{3/2}} \\ \frac{(x_1^2-2x_1x_2+x_2^2+y_1^2-2y_1y_2+y_2^2)}{\left(1-(z_1-z_2)^2/((x_1-x_2)^2+(y_1-y_2)^2+(z_1-z_2)^2)\right)^{1/2}\left((x_1-x_2)^2+(y_1-y_2)^2+(z_1-z_2)^2\right)^{3/2}} \\ 0 \\ 0 \\ 0 \end{bmatrix}^T \tag{40}$$

The $\widetilde{\boldsymbol{H}}$ matrix is mapped to the initial epoch t_0 through the State Transition Matrix (STM) as:

$$\boldsymbol{H}_k = \widetilde{\boldsymbol{H}}_k \boldsymbol{\Phi}(t_k, t_0) \tag{41}$$

where $\boldsymbol{\Phi}(t_k, t_0)$ is the STM from t_0 to t_k. The differential equation of the STM is given by:

$$\dot{\boldsymbol{\Phi}}(t_k, t_0) = A(\mathrm{t})\boldsymbol{\Phi}(t_k, t_0) = \frac{\partial F(X^*, t)}{\partial X}\boldsymbol{\Phi}(t_k, t_0) = \begin{bmatrix} 0_{3\times3} & \mathbf{I}_{3\times3} \\ \mathbf{G}(t) & 2\Omega \end{bmatrix}\boldsymbol{\Phi}(t_k, t_0) \tag{42}$$

where

$$\mathbf{G}(t) = \begin{bmatrix} \frac{\partial\ddot{x}}{\partial x} & \frac{\partial\ddot{x}}{\partial y} & \frac{\partial\ddot{x}}{\partial z} \\ \frac{\partial\ddot{y}}{\partial x} & \frac{\partial\ddot{y}}{\partial y} & \frac{\partial\ddot{y}}{\partial z} \\ \frac{\partial\ddot{z}}{\partial x} & \frac{\partial\ddot{z}}{\partial y} & \frac{\partial\ddot{z}}{\partial z} \end{bmatrix} \tag{43}$$

$$\Omega = \begin{bmatrix} 0 & 1 & 0 \\ -1 & 0 & 0 \\ 0 & 0 & 0 \end{bmatrix} \tag{44}$$

$$\boldsymbol{\Phi}(t_k, t_0) = \begin{bmatrix} \frac{\partial\mathbf{r}}{\partial\mathbf{r}_0} & \frac{\partial\mathbf{r}}{\partial\mathbf{v}_0} \\ \frac{\partial\mathbf{v}}{\partial\mathbf{r}_0} & \frac{\partial\mathbf{v}}{\partial\mathbf{v}_0} \end{bmatrix} \tag{45}$$

$$\boldsymbol{\Phi}(t_0, t_0) = I_{12\times12} \tag{46}$$

In general, Eq. 42 is computed numerically. On the other hand, analytical expressions require cumbersome work due to the complexity of these coupled equations. For the purpose of this work, we approximate the STM.

Basically, when $t - t_0$ is very small, the state transition matrix can be approximated by series expansion as shown below

$$\boldsymbol{\Phi}(t_k, t_0) = \begin{bmatrix} I & 0 \\ 0 & I \end{bmatrix} + \begin{bmatrix} 0 & I \\ G & 2\Omega \end{bmatrix}\Delta t + \begin{bmatrix} G & 2\Omega \\ 2\Omega G & G+4\Omega^2 \end{bmatrix}\frac{\Delta t^2}{2}$$
$$+ \begin{bmatrix} 2\Omega G & G+4\Omega^2 \\ G^2+4\Omega^2 G & 2\Omega G+2G\Omega+8\Omega^2 \end{bmatrix}\frac{\Delta t^3}{6}$$
$$+ \begin{bmatrix} G^2+4\Omega^2 G & 2\Omega G+4\Omega G\Omega+4G\Omega^2+16\Omega^3 \\ 2\Omega G^2+2G\Omega G+8\Omega^2 G & G^2+4\Omega^2 G+4\Omega G\Omega+4G\Omega^2+16\Omega^3 \end{bmatrix}\frac{\Delta t^4}{24} + \mathcal{O}(A^5) \tag{47}$$

where $\Delta t = t_k - t_0$. The Taylor expansion for the 3×3 position and velocity sub-matrices of the STM by ignoring the higher order terms are:

$$\Phi_{rr} = \frac{\partial\mathbf{r}}{\partial\mathbf{r}_0}$$
$$= I + G\frac{\Delta t^2}{2} + (2\Omega G)\frac{\Delta t^3}{6} + (G^2+4\Omega^2 G)\frac{\Delta t^4}{24} \tag{48}$$

$$\Phi_{rv} = \frac{\partial\mathbf{r}}{\partial\mathbf{v}_0}$$
$$= I\Delta t + \Omega\Delta t^2 + (G+4\Omega^2)\frac{\Delta t^3}{6}$$
$$+ (2\Omega G+4\Omega G\Omega+4G\Omega^2+16\Omega^3)\frac{\Delta t^4}{24} \tag{49}$$

$$\Phi_{vr} = \frac{\partial\mathbf{v}}{\partial\mathbf{r}_0}$$
$$= I + G\Delta t + \Omega G\Delta t^2 + (G^2+4\Omega^2 G)\frac{\Delta t^3}{6}$$
$$+ (2\Omega G^2+2G\Omega G+8\Omega^2 G)\frac{\Delta t^4}{24} \tag{50}$$

$$\Phi_{vv} = \frac{\partial\mathbf{v}}{\partial\mathbf{v}_0}$$
$$= 2\Omega\Delta t + (G+4\Omega^2)\frac{\Delta t^2}{2} + (2\Omega G+2G\Omega+8\Omega^2)$$
$$\times \frac{\Delta t^3}{6}$$
$$+ (G^2+4\Omega^2 G+4\Omega G\Omega+4G\Omega^2+16\Omega^3)\frac{\Delta t^4}{24} \tag{51}$$

Being G the gradient matrix at the end of the propagation interval. Finally, an approximation is performed by ignoring the remaining terms:

$$\boldsymbol{\Phi}(t_k, t_0) \approx \begin{bmatrix} \Phi_{rr} & \Phi_{rv} \\ \Phi_{vr} & \Phi_{vv} \end{bmatrix} \tag{52}$$

A performances comparison of Eq. 52 with respect to the numerically derived STM is given in Appendix B. It should be noted that Eq. 52 is given for only one of the spacecraft, requiring calculations for both spacecraft, $i = 1, 2$:

$$\Phi(t_k, t_0) = \begin{bmatrix} \Phi_1(t_k, t_0) & 0_{6\times6} \\ 0_{6\times6} & \Phi_2(t_k, t_0) \end{bmatrix} \quad (53)$$

$\widetilde{H}$ can be written in the following form of derivation with respect to the position and velocity vectors considering crosslink range observations:

$$\widetilde{H} = \begin{bmatrix} \frac{\partial \rho}{\partial \mathbf{r_1}} & \frac{\partial \rho}{\partial \mathbf{v_1}} & \frac{\partial \rho}{\partial \mathbf{r_2}} & \frac{\partial \rho}{\partial \mathbf{v_2}} \end{bmatrix} = \begin{bmatrix} \frac{\partial \rho}{\partial \mathbf{r_1}} & 0_{1\times3} & \frac{\partial \rho}{\partial \mathbf{r_2}} & 0_{1\times3} \end{bmatrix} \quad (54)$$

Now, we can directly calculate Eq. (41), $H_k = \widetilde{H}_k \Phi(t_k, t_0)$:

$$H = \widetilde{H}\Phi(t_k, t_0) = \begin{bmatrix} \frac{\partial \rho}{\partial \mathbf{r_1}} & 0_{1\times3} & \frac{\partial \rho}{\partial \mathbf{r_2}} & 0_{1\times3} \end{bmatrix}$$
$$\times \begin{bmatrix} \begin{bmatrix} \Phi_{1,rr} & \Phi_{1,rv} \\ \Phi_{1,vr} & \Phi_{1,vv} \end{bmatrix} & 0_{6\times6} \\ 0_{6\times6} & \begin{bmatrix} \Phi_{2,rr} & \Phi_{2,rv} \\ \Phi_{2,vr} & \Phi_{2,vv} \end{bmatrix} \end{bmatrix}$$
$$= \begin{bmatrix} \frac{\partial \rho}{\partial \mathbf{r_1}}\Phi_{1,rr} & \frac{\partial \rho}{\partial \mathbf{r_1}}\Phi_{1,rv} & \frac{\partial \rho}{\partial \mathbf{r_2}}\Phi_{2,rr} & \frac{\partial \rho}{\partial \mathbf{r_2}}\Phi_{2,rv} \end{bmatrix} \quad (55)$$

In Eq. 55, the velocity related terms for both spacecraft are $\frac{\partial \rho}{\partial \mathbf{r_1}}\Phi_{1,rv}$ and $\frac{\partial \rho}{\partial \mathbf{r_2}}\Phi_{2,rv}$ respectively. As it can be seen from Eq. 49, there is a null gradient matrix $G(t)$ related terms in Φ_{rv} till the third order expansion (e.g. $\Phi_{rv} = I\Delta t + \Omega\Delta^2$). This is why velocity related terms in H are linearly dependent at the second order approximation. On the other hand, many columns of $\widetilde{H}_k$ are equal in magnitude and opposite in sign, $\tilde{H}_k^1 = -\tilde{H}_k^7$ ($\frac{\partial \rho}{\partial x_1} = -\frac{\partial \rho}{\partial x_2}$). This would tend to make the rows of the information and observability matrices dependent A.Hill (2007). As stated in A.Hill (2007), the differences in the state transition matrix, $\Phi(t_k, t_0)$, when one of the spacecraft has a unique orbit, make H_k and thus the information and observability matrices positive definite. These differences can be seen, for example, in H_k^1 as partial derivatives of $\ddot{x}_1, \ddot{y}_1, \ddot{z}_1$ with respect to x_1 and in H_k^7 as partial derivatives of $\ddot{x}_2, \ddot{y}_2, \ddot{z}_2$ with respect to x_2. During the orbital trajectory, STM will be unique in cislunar vicinity and this will bring an observable system.

Now both Eq. 30, N and Eq. 31, Λ, can be built. By remembering that the inverse of the information matrix is nothing but the covariance matrix, $P = \Lambda^{-1}$. A priori covariance, P_0, may artificially make the system observable so that P_0 should not be added in the observability analysis. Lastly, the information matrix at t_k alone, $H^T W H$, in other words the effectiveness of observation at t_k, can be derived by using Eq. 55. For the observation effectiveness of the position states alone, x_i, y_i, z_i of the spacecraft $i = 1, 2$, can be calculated as:

$$\delta\Lambda_{\mathbf{r},ij}(t_k) = \frac{1}{\sigma_\rho}\sqrt{\text{row}_j\left(\Phi_{i,rr}^T(t_k, t_0)\right)\left(\frac{\partial \rho}{\partial \mathbf{r}_i}\right)^T\left(\frac{\partial \rho}{\partial \mathbf{r}_i}\right)\text{col}_j(\Phi_{i,rr}(t_k, t_0))} \quad (56)$$

and for the velocity states alone, x_i, y_i, z_i of the spacecraft $i = 1, 2$:

$$\delta\Lambda_{\mathbf{v},ij}(t_k) = \frac{1}{\sigma_\rho}\sqrt{\text{row}_j\left(\Phi_{i,rv}^T(t_k, t_0)\right)\left(\frac{\partial \rho}{\partial \mathbf{r}_i}\right)^T\left(\frac{\partial \rho}{\partial \mathbf{r}_i}\right)\text{col}_j(\Phi_{i,rv}(t_k, t_0))} \quad (57)$$

where subscript j indicates element number (e.g. $j = 1$ for x as a first state). As it can be seen, the observation effectiveness, thus the estimation accuracy, is directly related to the direction of observation and certain rows of the STM which is related to the divergent dynamics along a trajectory. Basically, STM approximates how a slight deviation in state variables propagates along the trajectory and it would be better from the estimation perspective if measurement vectors are not perpendicular to these deviations.

In this subsection $\widetilde{H}_k$ is given for range, range-rate, and LOS angle measurements. However, H_k is shown for the range measurement only case due to the complexity of other measurement models. The first element of $H_k^{\dot{\rho}_1}$ is given below as an example. In a similar way, other Jacobian matrices, $H_k^{\dot{\rho}}, H_k^{\phi}$ and H_k^{φ}, can be calculated.

$$H_k^{\dot{\rho}_1} = \left(\frac{\partial \ddot{x}_k}{\partial x_k}\frac{T_s^2}{2} + 1\right)\left(\frac{(\dot{x}_1 - \dot{x}_2)\rho^2 - (x_1 - x_2)\,\boldsymbol{\rho}\cdot\dot{\boldsymbol{\rho}}}{\rho^3}\right)$$
$$+ \left(\frac{\partial \ddot{y}_k}{\partial x_k}\frac{T_s^2}{2}\right)\left(\frac{(\dot{y}_1 - \dot{y}_2)\rho^2 - (y_1 - y_2)\,\boldsymbol{\rho}\cdot\dot{\boldsymbol{\rho}}}{\rho^3}\right)$$
$$+ \left(\frac{\partial \ddot{z}_k}{\partial x_k}\frac{T_s^2}{2}\right)\left(\frac{(\dot{z}_1 - \dot{z}_2)\rho^2 - (z_1 - z_2)\,\boldsymbol{\rho}\cdot\dot{\boldsymbol{\rho}}}{\rho^3}\right)$$
$$+ \left(\frac{\partial \ddot{y}_k}{\partial x_k}T_s^2 + \frac{\partial \ddot{x}_k}{\partial x_k}T_s\right)\left(\frac{(x_1 - x_2)}{\rho}\right)$$
$$+ \left(\frac{\partial \ddot{x}_k}{\partial x_k}T_s^2 + \frac{\partial \ddot{y}_k}{\partial x_k}T_s\right)\left(\frac{(y_1 - y_2)}{\rho}\right)$$
$$+ \left(T_s\frac{\partial \ddot{z}_k}{\partial x_k}\right)\left(\frac{(z_1 - z_2)}{\rho}\right) \quad (58)$$

5.2. Consider covariance analysis

For crosslink-based autonomous navigation systems, it is expected a certain level of bias in the radiometric measurements, predominantly because of the transmit and receive line delays on both spacecraft. Bias errors in the estimation process can be investigated in different ways. This can either be neglected or estimated by including dynamic or measurement model parameters into the state vector. Also, it can be considered by assuming bias is constant and its a priori estimate and associated covariance matrix are known. The consider approach is investigated in detail by many researchers (Lou et al. (2015); Montenbruck and Gill (2000); Grewal and Andrews (2008)). The consider covariance or filter analysis can be in a batch or in a sequential form. In this study, the sequential form of the consider filter is studied considering the

specific case of time-invariant measurement bias. This means the consider parameter $c_k = c_{k-1}$ for all k, and the bias covariance matrix P_k^{cc} is time-invariant. The sequential consider covariance filter or the Schmidt-Kalman filter (SKF) equations can be found in Lou et al. (2015).

5.3. Monte Carlo analysis

Monte Carlo methods are commonly used for sensitivity analysis and quantitative probabilistic analysis in navigation system design especially for analyzing errors. In this study, the Root Mean Square (RMS) error, in each kth time step, for the Nth case of the Monte Carlo simulation is calculated by using the following equation:

$$RMSE_k = \sqrt{\frac{1}{N}\sum_{i=1}^{N}(x_{i,k} - \hat{x}_{i,k})^2} \qquad (59)$$

where $x_{i,k}$ and $\hat{x}_{i,k}$ are ith component of state vector and its estimate respectively.

5.4. Observation type comparison

This study investigates the radiometric observables which are range, range-rate, and LOS angles. In order to test a navigation system, it should be studied which one of the observables provides better navigation performances for the same radio measurement system. In this section, the relation between radiometric observables will be given from the measurement precision point of view. In Section 3.3, it is already shown how LOS angles could be derived from range measurements. This is why in this section the relationship between range and range-rate measurements is given only. A quantitative approach is given in Dirkx et al. (2018) and a similar method has been used in this section. A Signal-to-Noise (SNR) criterion for an observable h (ρ or $\dot{\rho}$) and estimated states $\mathbf{X}$ can be given as:

$$SNR_{h,k} = \left| \frac{1}{\sigma_h} H_k \right| \qquad (60)$$

where σ_h is the noise level of the measurement h. Basically, we define the following figure of merit to compare the relative sensitivity of range and range-rate observables to estimated states $\mathbf{X}$:

$$\Xi_{\mathbf{X}} = \frac{SNR_\rho}{SNR_{\dot{\rho}}} \qquad (61)$$

If $\Xi_{\mathbf{X}} < 1$, it can be said that range-rate observation would become a feasible alternative to range observation for estimating $\mathbf{X}$. This can be applied to other states as well. The method given here can be considered as a ratio of the observability Gramian at each time epoch and multiplying it by a realistic relative measurement error parameter. Before making a realistic comparison, we would need to find the relation between range and range-rate observation errors, in other words, the relative error parameter. At first,

the ranging error will be defined. In case a conventional tone ranging is assumed for ranging operations, the following can be used to calculate the phase error on the major tone in radians:

$$\sigma_r = \sqrt{\frac{2B_n}{2\frac{S}{N_0}}} \qquad (62)$$

where $2B_n$ Bi-lateral loop bandwidth, S/N_0, signal-to-noise ratio in dB Hz. Basically, the phase noise on the major ranging tone results in a range measurement error by multiplying the wavelength of the ranging signal, $\lambda/2\pi$ as:

$$\sigma_\rho = \sigma_r \frac{\lambda}{2\pi} \qquad (63)$$

As an example, a 30dB Hz signal-to-noise ratio on the major tone with 0.1Hz loop bandwidth results in a 0.32m ranging error.

Doppler data noise can be expressed by the phase noise in radians and converted to range-rate noise by the following equation Montenbruck and Gill (2000):

$$\sigma_{\dot{\rho}} = \frac{\sqrt{2}c}{2\,G\,f_t\,t_c}\frac{\sigma_\varphi}{2\pi} \qquad (64)$$

with c speed of light, G transponding ratio, f_t, transmitted frequency, t_c, integration time, σ_φ phase noise in radians. Thus, the ratio of range and range-rate error, ζ, can be found by dividing Eq. 63–64:

$$\zeta = \frac{\sigma_\rho}{\sigma_{\dot{\rho}}} = \sqrt{2}\,G\,\frac{f_t}{f_{MT}}t_c \qquad (65)$$

As an example, for an S-band system, 1m ranging error would be equal to 0.3mm/s range-rate error with 1s integration on the same ranging/Doppler unit.

By using Eq. 65, it is possible to compare range only and range-rate only navigation systems in a realistic way. Now, Eq. 61 can be rewritten as:

$$\Xi_k^i = \frac{1}{\zeta}\left|\frac{H_\rho^i}{H_{\dot{\rho}}^i}\right| \qquad (66)$$

where i represents state number and k represents time.

6. Results

This section presents the effects of the various parameters on the performance of the autonomous navigation sys-
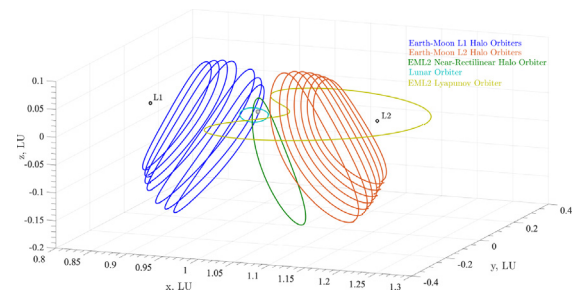

Fig. 8. Orbital trajectories considered in this study.

tem. Based on various orbital trajectories, shown in Fig. 8, measurement type, accuracy, bias, frequency, formation geometry, and network topology have been investigated.

6.1. Measurement type

Autonomous navigation system works well in cislunar space based on the previous studies. In order to illustrate that, in first, 14 days of simulation has been executed based on a link between L1 and L2 Halo orbiters considering a 1m ranging error (1σ). Corresponding estimation results can be seen in Fig. 9. Estimation errors are in order of 100m for position and 2mm/s for velocity after day 6. This represents that satellite-to-satellite tracking provides superior navigation performances in the lunar vicinity.

This section presents the effect of the different observation types (range, range-rate, and LOS angle) on the estimation performance. First, all three measurement types have been compared in the same scenario: one of the spacecraft orbits around the Moon and the second one has an Earth-Moon L2 Southern Halo orbit. Measurement precision has been adjusted in a realistic way by using Eq. 65 for range and range-rate, and Eq. 8 for LOS angles: the errors considered are 1m, 0.3mm/s, and 0.5deg, respectively. No bias has been assumed for measurement types. Fig. 10a shows the average position estimation error (including both spacecraft position states) for a Monte Carlo simulation (100 executions) including 3σ covariance bounds. The velocity estimation can be seen in Fig. 10b. The average position and velocity errors have been estimated by taking the mean value of the corresponding spacecraft states after running the RMS errors at each time step by using Eq. 59. As it can be seen, using range and range-rate observations provides the best state estimation results. On the other hand, having LOS angle measurements didn't improve the performances at all. As these LOS measurements contain high errors and range measurements provide more use-

ful data to the filter. Feeding the filter with very accurate LOS measurements slightly improves the navigation system performances, though. In the case a 0.001deg measurement error is considered (instead of 0.5deg), the RMS position and velocity estimation errors would be 57.54m and 0.92mm/s respectively. However, this would require a precise measurement system. This scenario illustrates what would happen in case other types of accurate LOS sensors had been considered. On the other hand, combining range and range-rate measurements improved the estimation performance by almost 10% as compared to range only. This means that for certain geometries, range-rate measurements provide useful information to the navigation filter. This improvement has also been observed in the velocity estimation as well. In addition, an EML1-L2 scenario has been investigated and all results can be seen in Table 1.

For the same scenario, the ratio Ξ has been plotted for the position states of the Earth-Moon L2 Halo orbiter, x_1, y_1, z_1, in Fig. 11 with a horizontal red line representing the overall mean value of them. As it can be seen, almost all the time, the ratio Ξ is higher than the threshold, ($\Xi > 1$). The average value of Ξ for this case can also be seen as 319.14, which means the range-only case with a measurement error of 1m provides better position estimation for the EML2 orbiter than the range-rate-only case with a measurement error of 0.3mm/s. On the other hand, the range-rate-only case provides better velocity estimation with a mean ratio Ξ of 0.28 (See Fig. 12). Considering other states, in brief, the range-only case shows better performance than the range-rate-only case.

In the second case, only range and range-rate measurements have been compared for different orbital configurations. In each different orbital scenario, four different cases have been investigated for a full orbital period. Based on 1m and 0.3mm/s measurement errors, Ξ_{mean} values are computed. All the mean results, Ξ_{mean}, are given in Table 2. All the results are higher than the threshold, $\Xi > 1$, which means
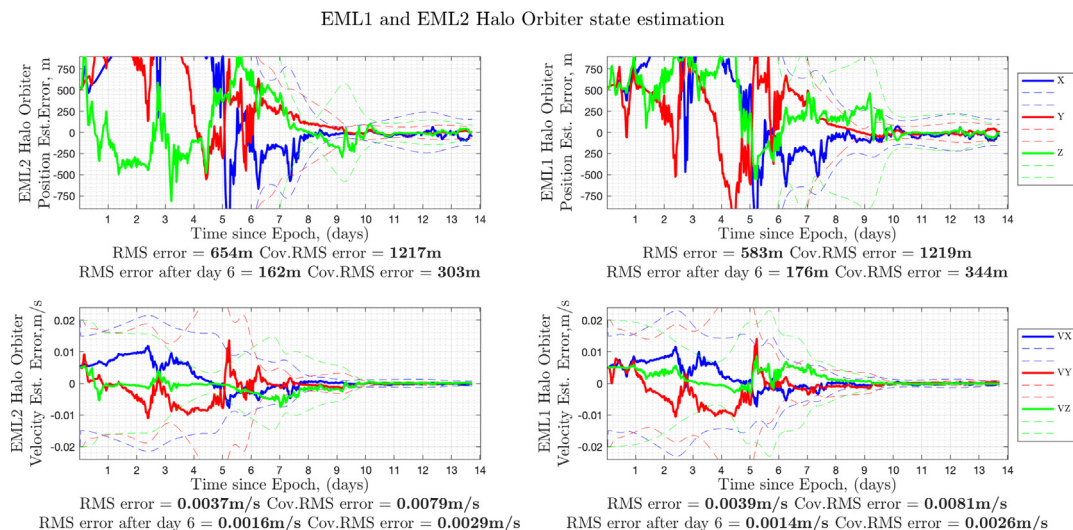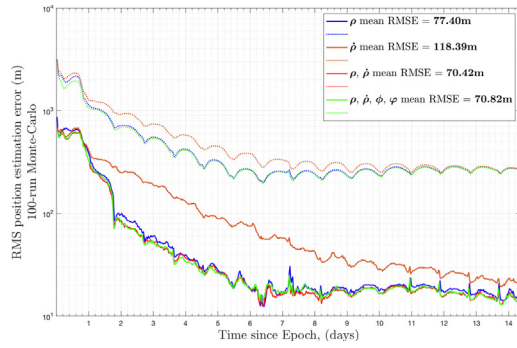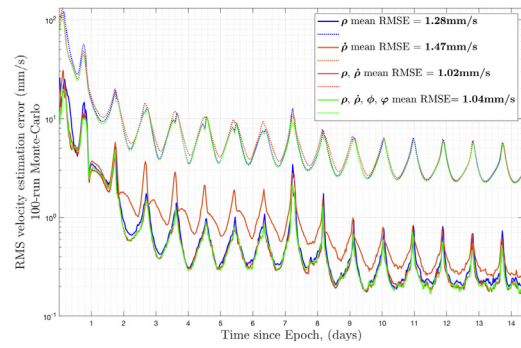

Fig. 9. EML1 and EML2 Halo Orbiter state estimation based on 1m ranging error.

(a) RMS position estimation error

(b) RMS velocity estimation error

Fig. 10. RMS state estimation error for four different measurement type scenario. The dashed lines represent 3σ covariance bounds.

Table 1
RMS State estimation errors based on 100 Monte-Carlo executions.

		EML1-L2 Orbiters	EML2-Lunar Orbiters
Range-only (ρ)	RMS Pos.Err. (m)	487.65	77.40
	RMS Vel.Err. (mm/s)	2.85	1.28
Range-rate-only ($\dot{\rho}$)	RMS Pos.Err. (m)	803.63	118.39
	RMS Vel.Err. (mm/s)	4.66	1.47
Range and range-rate ($\rho, \dot{\rho}$)	RMS Pos.Err. (m)	483.68	70.42
	RMS Vel.Err. (mm/s)	2.82	1.02
Range, range-rate and LOS ($\rho, \dot{\rho}, \phi, \varphi$)	RMS Pos.Err. (m)	486.14	70.82
	RMS Vel.Err. (mm/s)	2.85	1.04
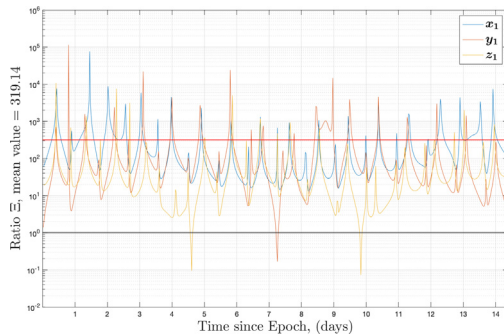
Fig. 11. Ratio Ξ values for position states of the Earth-Moon L2 Halo Orbiter. Horizontal black and red lines represent the threshold value and the mean value, respectively.
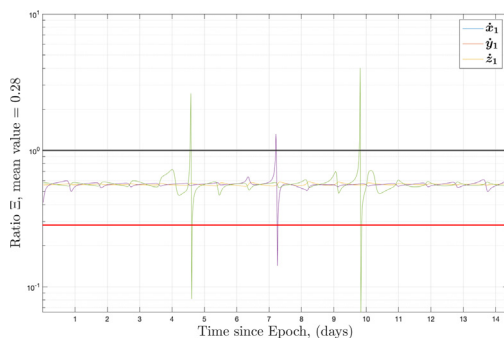
Fig. 12. Ratio Ξ values for velocity states of the Lunar Orbiter. Horizontal black and red lines represent the threshold value and the mean value, respectively.

range-only cases provide better overall state estimation than range-rate-only cases. A configuration in which spacecraft are located at EM L1 and L2 showed slightly higher Ξ_{mean} results than the other cases. This means that range-rate measurements would provide relatively less information to the filter than range measurements in case the formation is formed by spacecraft at both Lagrangian points. However, in case one of the spacecraft orbits around the Moon, range-rate measurements would provide relatively higher information than in the previous case. However, this still isn't sufficient for the range-rate-only case to have the same performance with respect to the range-only case.

Overall, range measurements would be more beneficial than range-rate measurements for radiometric autonomous navigation of cislunar small satellite formations. On the other hand, combining LOS angles with range measurements did not improve the navigation performance. This shows that crosslink range measurements are much better performing than angles as already noted in A.Hill (2007).

6.2. Measurement accuracy

This section represents the effects of measurement accuracy on the estimation performance for the selected orbital configurations. It is expected that higher measurement errors result in higher orbit determination errors. In order to see how the orbit determination performance changes with the increasing measurement errors, Monte Carlo simulations with 100 executions have been performed for

Table 2
Measurement type comparison for different orbital configurations.

	EML1/L2				EML1/Lunar				EML2/Lunar			
	$T_{2.786/3.306}$	$T_{2.778/3.276}$	$T_{2.759/3.240}$	$T_{2.721/3.195}$	$T_{2.786}$	$T_{2.778}$	$T_{2.759}$	$T_{2.721}$	$T_{3.306}$	$T_{3.276}$	$T_{3.240}$	$T_{3.195}$
Ξ_{mean}(1m/0.3mm/s)	289.21	365.53	510.73	219.14	182.65	155.05	221.02	75.31	110.86	116.50	167.17	116.25

various orbital configurations. In these simulations, range only and range-rate only cases have been investigated. Based on the link between two spacecraft at three different orbits, Earth-Moon L2 Southern Halo, L1 Southern Halo, Lunar, three different measurement accuracies for each measurement type (range, range-rate), 1m, 10m, 100m and 0.1mm/s, 1mm/s, 10mm/s, respectively, have been studied in this section.

The Monte Carlo based RMS position estimation results can be seen Figs. 13–15 for Earth-Moon L1-Lunar, Earth-Moon L2-Lunar, and Earth-Moon L1-L2 cases respectively. As it can be seen, higher measurement errors result in less accurate state estimation. Lunar and Lagrangian orbiter cases have almost the same order of magnitude position estimation errors. On the other hand, the EM L1-L2 case has higher estimation errors when the measurement errors are increasing. This is due to the fact that the system is less observable and the condition number and the unobservability index for both range and range-rate observations please see Table 3 for further details) are higher for this case than the others. Basically, less observable states are affected more in case of high measurement errors. Overall, highly observable orbital configurations, like the EML1-Lunar and the EML2-Lunar satellite formations, have been less affected by high measurement errors. This means that less precise inter-satellite measurement methods, such as time-derived or data-aided ranging, could be an option for these types of mission configurations considering the typical design challenges in small satellites Turan et al. (2022b).

6.3. Measurement bias

This section presents the effect of measurement bias on estimation performances. For this purpose, three different approaches have been studied: estimated bias, neglected bias, and considered bias. Two different simulation scenarios have been considered namely the EML2 and Lunar Elliptical Orbiter scenario and the EML1 and EML2 Orbiter scenario. In these simulations, in addition to a 3m, 1σ ranging error, a 30m ranging bias has been assumed. In the estimated bias case, the ranging bias has been estimated along with the dynamical states. In the considered bias case, the SKF has been studied. Basically, *a priori* estimate and associated covariance matrix of the measurement bias are known. Lastly, the neglected bias case ignored the measurement bias in the estimation process.

As shown in Fig. 16 and Fig. 17, the estimated and the considered bias approaches provide superior performances. However, neglecting the bias in the filter causes poor performance. This is more significant in the orbital configuration involving the Lunar Elliptical Orbiter. Basically, for a given relative motion, the measurement bias affects the estimation performance considerably and the high observable system involving the Lunar Orbiter allows to achieve of high performances if the measurement bias is estimated or considered in the navigation filter. In brief, ignoring the bias in the filtering process could cause poor navigation performances and might double the estimation error depending on the bias level. Note that low crosslink measurement errors (3m, 1σ) have been considered in the simulations. In the high measurement error case (100m, 1σ), the general trend in results would be the same. However, the consider approach would provide slightly better performance in this case. Lastly, regarding clock-related parameters, not only the clock bias but also drift and aging could be estimated in the navigation filter. However, expanding the number of estimated parameters could affect the observability of the system and thus the estimation performance.
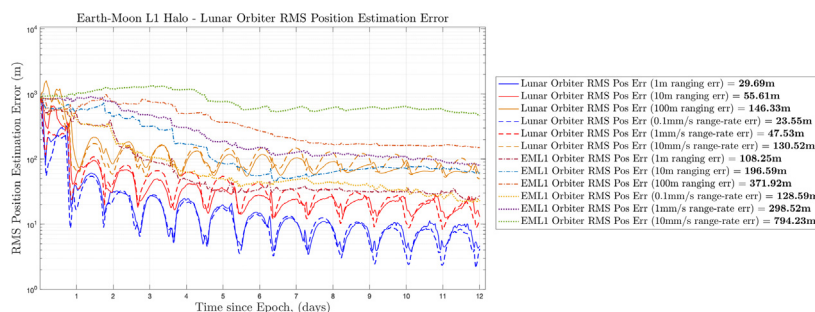
Fig. 13. The Earth-Moon L1 - Lunar Orbiter case RMS position estimation error for various range and range-rate measurement errors.
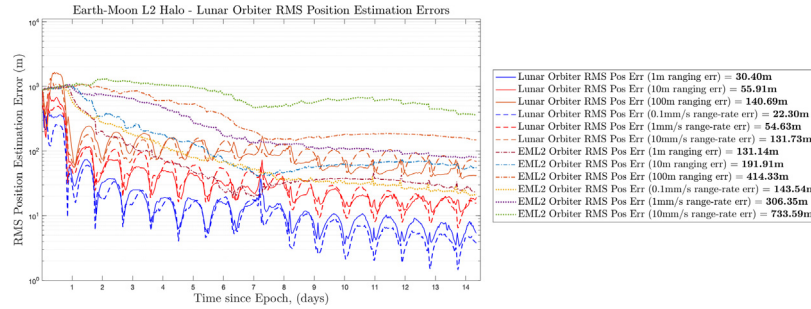
Fig. 14. The Earth-Moon L2 - Lunar Orbiter case RMS position estimation error for various range and range-rate measurement errors.
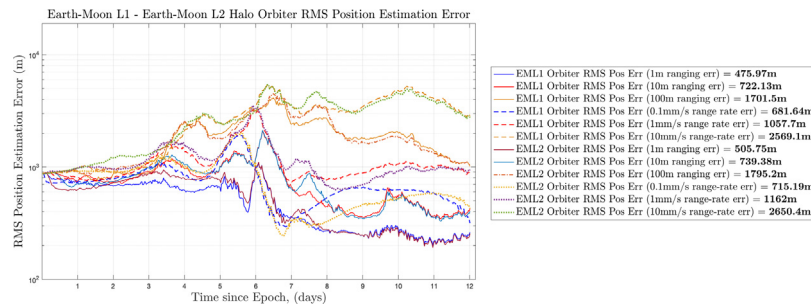
Fig. 15. The Earth Moon L1 - L2 Orbiter case RMS position estimation error for various range and range-rate measurement errors.

Table 3
Condition number and unobservability index for various measurement types and corresponding cases.

		EML1-Lunar	EML2-Lunar	EML1-L2
Cond.num	Range	1.34×10^{10}	1.10×10^{10}	3.57×10^{10}
	Range-rate	2.35×10^{10}	2.53×10^{10}	3.82×10^{10}
Unobs. index	Range	3.82×10^{2}	2.00×10^{2}	1.81×10^{4}
	Range-rate	0.2134	0.1756	2.84×10^{3}
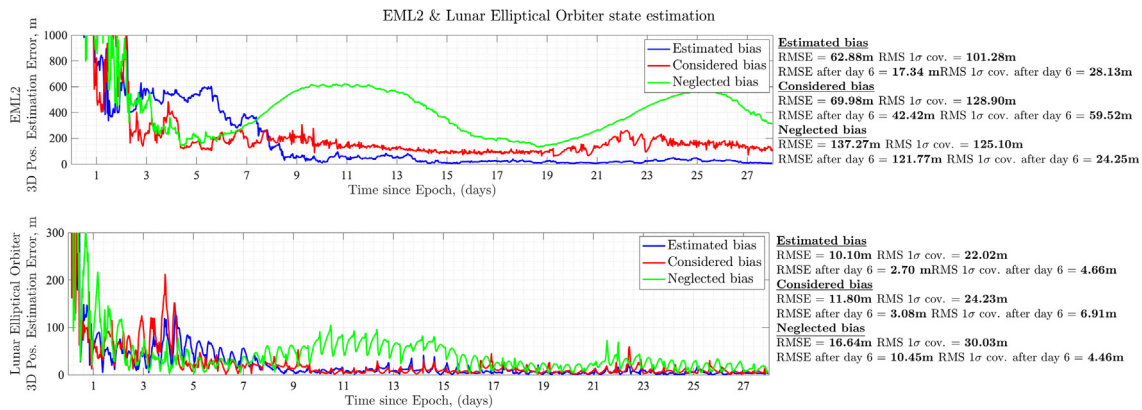
Fig. 16. 3D Position estimation error for the EML2 and Lunar Elliptical Orbiter scenario including a 30m ranging bias. Comparison of considered, estimated, and neglected bias cases.

6.4. Measurement frequency

It is expected that increasing the measurement interval would result in an increased time of filter convergence and increased RMS error with respect to the case of the same amount of time with high-frequency measurements.

To see how the orbit determination errors grow with low-frequency measurements, Monte Carlo simulations with 100 executions have been performed for various frequencies. This has been done based on the link between the EML1, L2 Halo Orbiters, and Lunar Orbiter considering a 1m, 1σ ranging error. Measurement intervals have been

Fig. 17. 3D Position estimation error for the EML1 and EML2 Orbiter scenario including a 30m ranging bias. Comparison of considered, estimated, and neglected bias cases.
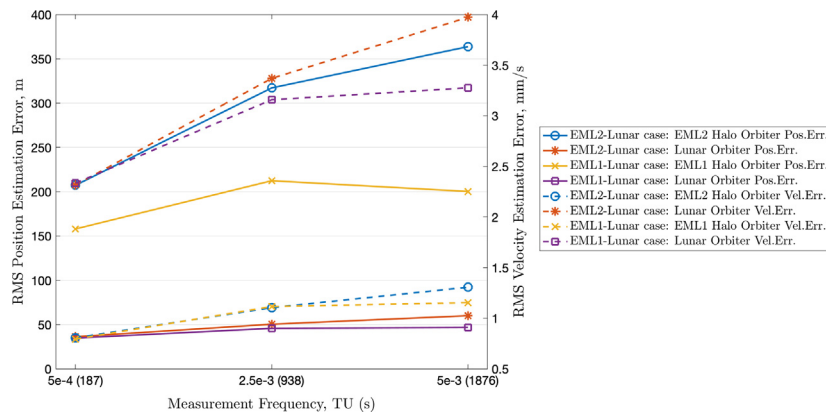
Fig. 18. The Earth-Moon L1 - L2 Orbiter case RMS position/velocity estimation errors for various measurement frequencies.

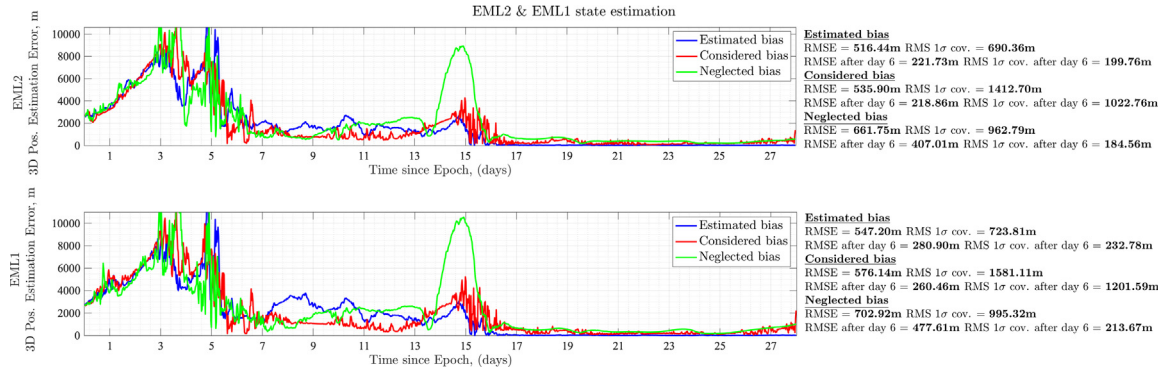set as 5×10^{-4}TU (187s), 2.5×10^{-3}TU (938s), and 5×10^{-3}TU (1876s). Corresponding results can be seen in Fig. 18.

As might be expected, high measurement intervals increase the RMS measurement error. On the other hand, the EML1-Lunar case showed that fewer measurements do not always mean having higher estimation errors. Basically, in the 1870s measurement interval case, measurements are collected in such a relative geometry that the navigation filter has been fed by more useful data than the case with a 938s measurement interval case. In addition, orbits with shorter periods (the Lunar Orbiter in these cases) are less sensitive to measurement interval changes.

Another important point related to measurement intervals is updating S/C states without measurements for a long time period. This situation could be the consequence of an issue in the satellite formation resulting in a time window without any measurements. Basically, if states are updated without measurements after reaching a converged navigation solution (typically after day 6–7 for the selected scenarios), RMS 1σ position uncertainty after day 6 would be 194m and 116m for EML2 and Lunar orbiters, respectively (a scenario based on the crosslink between the EML2 and the Lunar orbiters for the duration of 14 days). The results would be 80m and 12m if measurements are

collected continuously during the full 14 days of simulation. However, in the EML1 and EML2 case, averaged uncertainty would increase from around 400m to almost 4000m for both S/C. This represents that if the satellite formation is formed by only Halo orbiters, states must be updated via measurements with shorter time intervals. Note that this finding could be more significant in the analysis based on the high-fidelity dynamical model including modeling errors due to gravitational perturbations.

6.5. Formation geometry

In this section, the effect of the relative geometry between satellites has been investigated. This was done by changing the orbital period of the Lagrangian orbiters at the Earth-Moon L1 and L2. This eventually affects the inter-satellite distance and thus the relative geometry. Different constellation geometries, coplanar and non-coplanar cases at the Lagrangian points, have been investigated in A. Hill (2007) and it was shown that the autonomous orbit determination would not work for close formations but only for those with large separations. This section will study the formation geometry from the observability perspective for formations located at different Lagrangian points.

Fig. 19. Condition number variation among various L1 and L2 Orbiters.

Fig. 21. Condition number variation among various L1 and L2 Orbiters based on range-rate measurements.

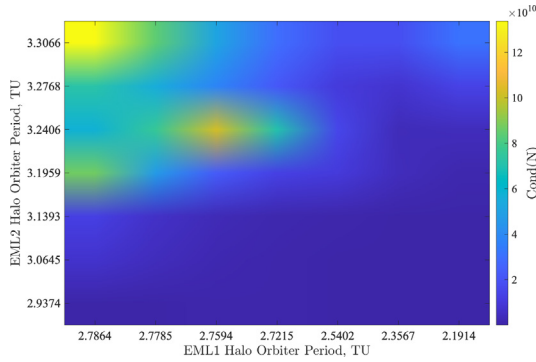Simulations have been configured such that one of the spacecraft has an EML1 Halo orbit and the second one has an EML2 Halo orbit. In the first case, all possible crosslink scenarios between seven EM L1 and EM L2 Halo orbiters have been simulated. In these cases, the inter-satellite distances have been changed from a minimum of 18411km to a maximum of 133738km. The duration of the simulations has been adjusted based on the period of the spacecraft with the longest orbital period, ranging between 12.75 days and 14.36 days. Fig. 19 shows the condition number variation among the various L1 and L2 orbiters. It can be seen that the system becomes less observable when both spacecraft have longer orbital periods and more observable when both have shorter periods or one of them has a short and the other one has a longer period. Basically, shorter orbital periods have higher relative velocity (see the Fig. 20 for further details) and spacecraft with a shorter period can obtain more information while spacecraft with a longer period completes its one orbital period. On the other hand, Lagrangian orbiters with shorter periods are in general close to the Moon and their orbital plane becomes planar, allowing them to collect more information in the x-y plane. In the case of range-rate observations, the results did not change from those provided in Fig. 21.

In the second run, the crosslink between EM L2 Halo orbiter and the Lunar orbiter has been investigated. The same trends have been observed in this case and the corresponding results are provided in Fig. 22.

Fig. 22. Condition number and minimum relative distance variation among various L2 and Lunar Orbiter.

6.6. Network topology

In case there are more than two spacecraft in the system, the network topology would become an important parameter to consider. Increasing the number of spacecraft, thus increasing the number of inter-satellite links, would improve the overall navigation performance. This is due to the increase in information acquired at the same time, thanks to the different relative geometries between spacecraft. In this section, triple spacecraft scenarios have been investigated considering two different network topologies: centralized (star) and distributed (mesh). The centralized, or in other words star topology, has a simple design advantage, but it has a single point of failure. On the other hand, distributed or mesh topologies supports interactions among all spacecraft but they suffer from complexity as the number of spacecraft and links increases. These different scenarios are listed in Table 4 and 5.

In the centralized topology, the very first three scenarios have the same relative geometry, but different central nodes (mothercraft), which results in different inter-satellite measurement vectors. In other words, the mothercraft collects observations in each centralized scenario. This will show the effect of the orbital period on the overall navigation performances. The last three scenarios have the same spacecraft as a central node but different configurations

Fig. 20. Mean relative velocity between spacecraft among various L1 and L2 Orbiters.

Table 4

Triple spacecraft scenarios for the centralized topology.

Scenario ID	Triple Spacecraft Configurations - Centralized Topology	
	Central node	Deputies
C1	EML2 Halo	EML1 Halo - Lunar Orbiter
C2	EML1 Halo	EML2 Halo - Lunar Orbiter
C3	Lunar Orbiter	EML2 Halo - EML1 Halo Orbiter
C4	EML2 Halo	EML2 Halo (non-coplanar) - Lunar Orbiter
C5	EML2 Halo	EML2 NRHO - Lunar Orbiter
C6	EML2 Halo	EML2 Lyapunov - Lunar Orbiter

Table 5

Triple spacecraft configurations - mesh topology.

Scenario ID	Triple Spacecraft Configurations - Mesh Topology
M1	EML2 Halo - EML1 Halo - Lunar Orbiter
M2	EML2 Halo - EML2 Halo (non-coplanar) - Lunar Orbiter
M3	EML2 Halo - EML2 NRHO - Lunar Orbiter
M4	EML2 Halo - EML2 Lyapunov - Lunar Orbiter

of deputies (daughtercraft). This will allow observing the effect of different relative geometries/inter-satellite distances.

In the mesh topology scenarios, all the spacecraft have measurements between each other. The first scenario is nothing but the mesh version of the very first three scenarios previously presented. The last three scenarios are the mesh version of the corresponding centralized topology. These scenarios will show the effect of having an additional inter-satellite link on the overall navigation performance.

All the centralized and mesh topology RMS position estimation errors (three S/C position errors have been averaged over 100 Monte Carlo executions) can be seen in Fig. 23a and 23b, respectively. RMS position and velocity estimation errors for both centralized and mesh topologies can be seen in Table 6 and Table 7. The unobservability index for the centralized and mesh topology scenarios can be seen in Table 8 and 9, respectively.

Considering the very first three centralized scenarios (C1, C2, C3), a central node having a shorter orbital period, a lunar orbiter (C3), provides better estimation accu-

racy than a mothercraft located at the Lagrangian points (C1, C2). This is due to the fact that the Lunar orbiter had better observation geometry and collected all the information in a shorter time. In addition, this case (C3) has a lower unobservability index than the other cases. On the other hand, the results of the last three centralized scenarios showed that larger inter-satellite distances provide better state estimation. Comparing C2 with C4 shows that having a shorter inter-satellite link in the topology decreases the overall navigation system performance.

Regarding the mesh scenarios, the first case (M1) showed that adding an additional link, thus measurement, on a centralized scenario (C1, C2, C3) improved the navigation performances. This behavior has been observed in other cases as well by comparing M2, M3, and M4 with C2, C3, and C4. As it can be seen, M3 converges faster than M4 showing that shorter orbital periods (T = 7.94 days, T = 18.71 days) in the formation provide a quicker solution. The reason is that the filter in this case is fed by observations containing information about the full orbital trajectory and not just a sub-section.

Finally, the largest axis of the 3D, 3σ error ellipsoid for each S/C at each time step averaged over the entire time span was used to evaluate the estimation performance of both network topologies. All different mesh and centralized topology combinations have been investigated for a total of 7 S/C. In this case, the mesh topology has a combination of 7 orbital configurations taken 3 at a time without repetition and this gives $\binom{7}{3} = 35$ combinations. For the centralized network topology, as an extra, a central node must be

(a) Centralized Topology   (b) Mesh Topology

Fig. 23. RMS position estimation error for network topology scenarios.

Table 6
RMS Estimation errors for various centralized topologies.

	C1	C2	C3	C4	C5	C6
RMS Pos.Error (m)	98.37	76.93	57.82	141.01	123.56	153.57
RMS Vel.Error (mm/s)	1.15	0.97	0.71	1.43	1.32	1.37

Table 7
RMS Estimation errors for various mesh topologies.

	M1	M2	M3	M4
RMS Pos.Error (m)	41.16	99.18	85.79	105.31
RMS Vel.Error (mm/s)	0.63	1.03	0.88	0.91

Table 9
Unobservability index for mesh topology scenarios.

	M1	M2	M3	M4
$1/\min(eig(N))$	1.25×10^2	1.52×10^2	1.36×10^2	1.96×10^2

selected from each S/C non-repetitive combination, so this results in a total number of $35 \times 3 = 105$ combinations. For this analysis, simulation time has been set to 28 days and a circular lunar orbiter has also been studied to show the effects of a circular orbit. The results of all these combinations can be found in Fig. 24a and Fig. 24b for the centralized and the mesh network topologies, respectively. As it can be seen, in general, the centralized topology combinations formed by either lunar elliptical or polar circular orbiters provide the best performances among all combinations. In addition, combinations formed by the Lunar elliptical orbiter provide slightly better overall navigation performances than the Lunar polar-circular orbiter (particularly on the velocity estimation). This is due to the fact that circular orbital configurations might affect the observability of the system. On the other hand, if the centralized network topology is formed only by L1 or L2 Halos, then it would produce a poor navigation solution. Regarding the mesh topology, again, the additional inter-satellite link

provides a better navigation solution. Once again, the best performances have been achieved with the mesh topology formed by the Lunar orbiters. Generally, the mesh topologies formed by Halo orbiters have taken advantage the most from the additional inter-satellite link. The navigation system in the mesh topology is fed by observations providing more valuable information. Basically, each S/C state is estimated by two different measurement vectors at a time and the navigation filter uses the most effective observation from them. The angle between the intersatellite measurement vector and the axis of most uncertainty could be useful to understand this point. If this angle is small, then the observation would provide more useful information (measurements are in the same direction of the axis of most uncertainty). In short, the navigation system in the mesh topology could have the option to use better observables. In a similar way, on-board decisions, such as on-board measurement planning, can be made based on this information.

Table 8
Unobservability index for centralized topology scenarios.

	C1	C2	C3	C4	C5	C6
$1/\min(eig(N))$	2.97×10^2	7.74×10^2	1.91×10^2	4.5×10^2	3.54×10^2	3.85×10^2

(a) Centralized Network Topology

(b) Mesh Network Topology

Fig. 24. Averaged position uncertainties for the centralized and the mesh network topologies.

7. Limitations

The findings of this study should be considered in light of some limitations: primarily, the generalization of these results is related to the orbital dynamics used in this study. Basically, a performance analysis of the autonomous orbit determination method has been conducted considering CRTBP as a dynamical model without any error. The results obtained via the simple dynamics are required to be verified under a realistic model including spherical harmonics of the gravity field and solar radiation pressure. Based on the previous studies, state estimation errors remain at the same order of magnitude for CRTBP and the ephemeris model in the lunar vicinity A.Hill (2007); Turan et al. (2022a). However, propagation errors must be taken into account. For practical applications, it is recommended to consider spherical harmonics of the Moon's gravity field expanded to the 12th order and degree, Earth and Sun as point masses, and solar radiation pressure for a lunar elliptical orbiter to keep the expected propagation error below 1km after a day Scotti et al. (2022). In addition, considering the 30th order and degree spherical harmonics of the Moon's gravity would keep the expected propagation error below a km level after two weeks for both a lunar elliptical and an Earth-Moon L2 Halo orbiter Tanis (2022). Considering the findings of this study, in brief, the results would be quantitatively different for the relation between measurement precision/accuracy and the estimation performance, given in the Section 6.2, if the dynamics were changed. In this case, the navigation filter would provide a less accurate solution and this would be more significant if the filter is fed by measurements with high errors. Also note that expanding the number of estimated parameters (including clock related parameters, radiation pressure coefficient, and other coefficients) could affect the observability of the system and thus the estimation performance. In addition, updating S/C states without measurements due to line-of-sight visibility limitations may lead to higher state errors in the high-fidelity dynamics than in a simple dynamical model and this would produce quantitatively different results given in the measurement frequency section. However, the results related to the observation geometry, such as formation geometry or network topology as well as measurement type, would be less affected if the high-fidelity dynamical model were considered.

The second limitation concerns the low number of halo orbits considered in this work, leaving the detailed investigation to the future including a study on different orbital phase angles and co-planar orbital configurations.

The research only considered constant measurement noise and process noise matrices in the estimation process. However, adaptive estimation techniques, or in other words, adaptive adjustment of noise covariance, has also been implemented and tested in previous studies. It has been found that there has been no significant difference between constant noise covariance matrices and adaptive adjustment of noise covariance on the navigation performance in the case of simple orbital dynamics. This would not be the case in the high fidelity models. Lastly, clock-related parameters such as bias, drift, and aging and their effects have not been considered in this study except for the bias in the measurement bias section. These parameters could affect the results in the longer duration of simulations.

8. Conclusion

The aim of this study was to investigate the effect of different aspects on the performances of a crosslink radiometric measurement-based autonomous navigation method for the special case of cislunar small satellite formations. Various crosslink radiometric data types have been presented including their expected performances. Thereafter, orbit determination models and various performance analysis methods were given. The navigation system performances have been studied to quantify the effects of important parameters including measurement type, accuracy, bias, frequency, formation geometry, and network topology. It was found that range observation type provides a better state estimation than range-rate observables for the autonomous navigation system in cislunar space. Adding LOS measurements into the filter provided better results for the mission scenarios presented in the research only if LOS measurements are precise (less than 3.6arcsec, 1σ), which is difficult to achieve in practice via radio-interferometric methods on small satellites. On the other hand, combining range and range-rate observables slightly improved the estimation performance. Instead of combining them, one approach would be investigating the observation effectiveness for each observation type and using range or range-rate only measurements in the best tracking windows. Regarding measurement precision, highly observable orbital configurations are less affected by high measurement errors. This means that less precise inter-satellite measurement methods, such as telemetry-based, time-derived, or data-aided ranging, could be an option for these formations. As might be expected, high measurement intervals increase the state estimation uncertainty. In addition, Halo-only satellite formations require more frequent measurements. Regarding the formation geometry, orbiters with two shorter periods or one shorter and one longer period presented better observable systems. In case there are more than two spacecraft in the system, the mesh topology provided better state estimations and quicker converged navigation solutions than a centralized topology, as expected, due to the increased number of measurements and better measurement geometries. However, considering the overall system performance, it would be beneficial for the centralized topology to collect all the measurements on the spacecraft with the shortest orbital period. In general, the network topologies consisting of large inter-satellite links and short orbital periods would benefit most from autonomous orbit determination.

Declaration of Competing Interest

The authors declare that they have no known competing financial interests or personal relationships that could have appeared to influence the work reported in this paper.

Appendix A. This part represents the required calculations for the variance of the LOS measurements derived from time-delay and phase-shift radiometric measurement approaches. Recall that the variance of a continuous random variable X is defined as:

$$\text{Var}[X] = \text{E}\left[(X - \text{E}[X])^2\right] = \text{E}[X^2] - (\text{E}[X])^2 \tag{A.1}$$

for constants a and b:

$$\text{Var}[a + bX] = b^2 \text{Var}[X] \tag{A.2}$$

Taking the variance of both hand sides of Eq. 6 for the time-delay-based approach:

$$\text{Var}[\Delta t] = \frac{b^2}{c^2} \text{Var}[\cos \psi] \tag{A.3}$$

A variance of $\cos \psi$ is given as:

$$\text{Var}[\cos \psi] = \text{E}\left[\cos^2 \psi\right] - (\text{E}[\cos \psi])^2 \tag{A.4}$$

where

$$\text{E}[\cos \psi] = \sum_{k=0}^{\infty} \frac{(-1)^k}{2k!} \text{E}\left[\psi^{2k}\right]$$
$$= \sum_{k=0}^{\infty} \frac{(-1)^k}{2k!} \sigma^{2k}(2k-1)! = e^{-\sigma_\psi^2} \tag{A.5}$$

and

$$\text{E}\left[\cos^2 \psi\right] = 1 - \text{E}\left[\sin^2 \psi\right]$$
$$= 1 - \left(\frac{1}{2}(1 - \text{E}[\cos 2\psi])\right)$$
$$= 1 - \left(\frac{1}{2}\left(1 - \sum_{k=0}^{\infty}(-1)^k \frac{2^{2k}}{2k!} \text{E}\left[\psi^{2k}\right]\right)\right) \tag{A.6}$$

$$\text{E}\left[\cos^2 \psi\right] = 1$$
$$- \left(\frac{1}{2}\left(1 - \sum_{k=0}^{\infty}(-1)^k \frac{2^{2k}}{2k!} \sigma^{2k}(2k-1)!\right)\right)$$
$$= 1 - \left(\frac{1 - e^{-2\sigma_\psi^2}}{2}\right) = \left(\frac{1 + e^{-2\sigma_\psi^2}}{2}\right) \tag{A.7}$$

Inserting Eq. A.5 and A.7 into A.4 results in:

$$\text{Var}[\Delta t] = \frac{b^2}{c^2}\left(\left(\frac{1 + e^{-2\sigma_\psi^2}}{2}\right) - e^{-2\sigma_\psi^2}\right)$$
$$= \frac{b^2}{c^2}\left(\frac{1 - e^{-2\sigma_\psi^2}}{2}\right) \tag{A.8}$$

This can also be written in terms of ranging errors:

$$\sigma_\rho = b\sqrt{\frac{1 - e^{-2\sigma_\psi^2}}{2}} \tag{A.9}$$

or

$$\sigma_\psi = \sqrt{ln\left(\frac{1}{\sqrt{1 - \frac{2\sigma_\rho^2}{b^2}}}\right)} \tag{A.10}$$

Similarly, the relation between phase-shift measurement error and line-of-sight measurement error can be found by taking the variance of both hand sides of Eq. (7):

$$\text{Var}[\tau] = \frac{(2\pi b)^2}{\lambda^2} \text{Var}[\sin \psi] \tag{A.11}$$

Since a zero-mean Gaussian with variance σ_ψ^2 is assumed ($\text{E}[\sin \psi] = 0$), the variance of $\sin \psi$ is given as:

$$\text{Var}[\sin \psi] = \text{E}\left[\sin^2 \psi\right] = \frac{1}{2}(1 - \text{E}[\cos(2\psi)])$$
$$= \frac{1 - e^{-2\sigma_\psi^2}}{2} \tag{A.12}$$

This can be written as:

$$\sigma_\tau = \frac{2\pi b}{\lambda}\sqrt{\frac{1 - e^{-2\sigma_\psi^2}}{2}} \tag{A.13}$$

or

$$\sigma_\psi = \sqrt{ln\left(\frac{1}{\sqrt{1 - \frac{2\sigma_\rho^2 \lambda^2}{(2\pi b)^2}}}\right)} \tag{A.14}$$

It is also can be seen in the phase-shift measurement approach that line-of-sight measurements would not be possible if $\sigma_\tau < \frac{\sqrt{2}\pi b}{\lambda}$ is not met. As a side note, time-delay and phase-shift measurements can be invertable as $\sigma_{\Delta t} = \sigma_\tau \lambda/2\pi c$

Appendix B. In this section, the state transition matrix generated by the numerical integrator (ODE113 in Matlab) used as a reference is compared with the state transition matrix approximated by the method given in subSection 5.1. Based on the following relative error parameter,

$$\epsilon = \frac{1}{36}\sum_{i=1}^{6}\sum_{j=1}^{6}\left|\frac{(\mathbf{\Phi}_{ij} - \bar{\mathbf{\Phi}}_{ij})}{\mathbf{\Phi}_{ij}}\right| \tag{B.1}$$

where $\bar{\mathbf{\Phi}}_{ij}$ and $\mathbf{\Phi}_{ij}$ represent the STM calculated by the numerical integrator and approximated method respectively. A comparison has been made based on two different orbits, namely Earth-Moon L2 and Earth-Moon L1 Southern Halo for 7 days of duration. RMS errors and their

Table B.10
Performance investigation of the approximated STM.

$\Delta t(s)$	ϵ for EM L2 orbiter		ϵ for EM L1 orbiter	
	RMSE	1σ STD	RMSE	1σ STD
10	9.29×10^{-10}	7.54×10^{-10}	1.75×10^{-9}	1.13×10^{-9}
60	6.44×10^{-9}	1.64×10^{-8}	1.22×10^{-8}	2.83×10^{-8}
100	1.42×10^{-8}	3.89×10^{-8}	2.65×10^{-8}	6.70×10^{-8}
600	6.95×10^{-8}	5.54×10^{-7}	1.31×10^{-7}	9.68×10^{-7}

standard deviations for various step sizes are given in Table B.10.

References

A.Hill, K., 2007. Autonomous Navigation in Libration Point Orbits. University of Colorado, Ph.D. thesis.

Andrews, K., Hamkins, J., Shambayati, S., Vilnrotter, V., 2010. Telemetry-based ranging. In: 2010 IEEE Aerospace Conference. IEEE, pp. 1–16. https://doi.org/10.1109/AERO.2010.5446926.

Asmar, S.W., Armstrong, J.W., Iess, L., Tortora, P., 2005. Spacecraft Doppler tracking: Noise budget and accuracy achievable in precision radio science observations. Radio Sci. 40 (2), 1–9. https://doi.org/10.1029/2004rs003101.

Benedetto, M.D., Imperi, L., Durante, D., Dougherty, M., Iess, L., Notaro, V., Racioppa, P., 2019. Augmenting NASA Europa Clipper by a small probe: Europa Tomography Probe (ETP) mission concept. Acta Astronaut. 165, 211–218. https://doi.org/10.1016/j.actaastro.2019.07.027.

Bentum, M., Boonstra, A.-J., Klein Wolt, M., Brinkerink, C., Alpay Koc, N., Fuster, S., Kumar, R., Prinsloo, D., Verhoeven, C., Verma, M., 2018. The CubeSat Low Frequency Explorer (CLE) in Lunar Orbit. In: 42nd COSPAR Scientific Assembly. vol. 42.

Burgett, B., Long, J., Whaley, P., Raz, A., Herrick, R., Thorsen, D., Delamere, P., 2016. Mini-MAGGIE: CubeSat MAGnetism and Gravity Investigation at Europa. In: 47th Lunar and Planetary Science Conference, pp. 1–2. https://www.hou.usra.edu/meetings/lpsc2016/pdf/1928.pdf.

CCSDS, 2013. Proximity-1 Space Link Protocol - Physical Layer CCSDS 211.1-B-4. Technical Report. https://public.ccsds.org/Pubs/211x1b4e1.pdf.

CCSDS, 2014. Pseudo-Noise (PN) Ranging Systems CCSDS 414.0-G-2. Technical Report. https://public.ccsds.org/Pubs/414x0g2.pdf.

Cervone, A., Topputo, F., Speretta, S., Menicucci, A., Turan, E., Lizia, P. D., Massari, M., Franzese, V., Giordano, C., Merisio, G., Labate, D., Pilato, G., Costa, E., Bertels, E., Thorvaldsen, A., Kukharenka, A., Vennekens, J., Walker, R., 2022. LUMIO: A CubeSat for observing and characterizing micro-meteoroid impacts on the lunar far side. Acta Astronaut. 195, 309–317. https://doi.org/10.1016/j.actaastro.2022.03.032.

Cheetham, B., 2021. Cislunar Autonomous Positioning System Technology Operations and Navigation Experiment (CAPSTONE). In: ASCEND 2021. American Institute of Aeronautics and Astronautics, pp. 1–8. https://doi.org/10.2514/6.2021-4128.

Curtis, H., 2020. Orbital Mechanics for Engineering Students. Elsevier Ltd, Oxford, https://www.ebook.de/de/product/41219397/howard_curtis_orbital_mechanics_for_engineering_students.html.

Daniel, J.G., 2006. Generating Periodic Orbits in the Circular Restricted Three-Body Problem with Applications to Lunar South Pole Coverage. Purdue University, West Lafayette, Indiana, Master's thesis MSc thesis.

Dianetti, A.D., Weisman, R.M., Crassidis, J.L., 2017. Application of observability analysis to space object tracking. In: AIAA Guidance, Navigation, and Control Conference. American Institute of Aeronautics and Astronautics, pp. 6–7. https://doi.org/10.2514/6.2017-1258.

Dirkx, D., Prochazka, I., Bauer, S., Visser, P., Noomen, R., Gurvits, L.I., Vermeersen, B., 2018. Laser and radio tracking for planetary science missions—a comparison. J. Geodesy 93 (11), 2410–2411. https://doi.org/10.1007/s00190-018-1171-x.

DSN, 2018. DSN Telecommunications Link Design Handbook, 810-005. Technical Report Jet Propulsion Laboratory California Institute of Technology. URL http://deepspace.jpl.nasa.gov/dsndocs/810-005/.

Fehse, W., 2003. Automated Rendezvous and Docking of Spacecraft. Cambridge Aerospace Series. Cambridge University Press, The Edinburgh Building, Cambridge, United Kingdom. https://doi.org/10.1017/CBO9780511543388.

Fujimoto, K., Leonard, J., Mcgranaghan, R., Parker, J., Anderson, R., Born, G., 2012. Simulating the LiAISON Navigation Concept in GEO + Earth-Moon Halo Constellation. In: 23rd International Symposium on Space Flight Dynamics, Pasadena, California, pp. 1–15, URL https://hdl.handle.net/2014/43020.

Fujimoto, K., Stacey, N., Turner, J.M., 2016. Stereoscopic Image Velocimetry as a Measurement Type For Autonomous Asteroid Gravimetry. In: AIAA/AAS Astrodynamics Specialist Conference. American Institute of Aeronautics and Astronautics, pp. 1–12. https://doi.org/10.2514/6.2016-5566.

Gao, Y., Xu, B., Zhang, L., 2014. Feasibility study of autonomous orbit determination using only the crosslink range measurement for a combined navigation constellation. Chin. J. Aeronaut. 27 (5), 1199–1210. https://doi.org/10.1016/j.cja.2014.09.005.

Goldberg, H.R., Karatekin, Ö., Ritter, B., Herique, A., Tortora, P., Prioroc, C., Gutierrez, B.G., Martino, P., Carnelli, I., 2019. The Juventas CubeSat in Support of ESA's Hera Mission to the Asteroid Didymos. In: AIAA/USU Conference on Small Satellites. Utah State University, Logan, UT, pp. 1–7, URL https://digitalcommons.usu.edu/smallsat/2019/all2019/73/.

Grewal, M., Andrews, A., 2008. Kalman Filtering: Theory and Practice Using MATLAB, (3rd ed.). John Wiley & Sons Inc, Hoboken, New Jersey. https://doi.org/10.1002/9780470377819.

Hamkins, J., Kinman, P., Xie, H., Vilnrotter, V., Dolinar, S., 2015. Telemetry Ranging: Concepts. IPN Progress Report 42–203, pp. 1–20. https://ipnpr.jpl.nasa.gov/progress_report/42-203/203C.pdf.

Hesar, S., Parker, J., Mcmahon, J., Born, G., 2015. Small Body Gravity Field Estimation Using LiAISON Supplemented Optical Navigation. In: 38th Annual AAS Rocky Mountain Section Guidance and Control Conference Conference, Breckenridge CO, pp. 41–54.

Hill, K., Born, G.H., 2007. Autonomous Interplanetary Orbit Determination Using Satellite-to-Satellite Tracking. J. Guidance Control Dyn. 30 (3), 679–686. https://doi.org/10.2514/1.24574.

Hill, K., Parker, J., Born, G., Demandante, N., 2006. A Lunar L2 Navigation, Communication, and Gravity Mission. In: AIAA/AAS Astrodynamics Specialist Conference and Exhibit. American Institute of Aeronautics and Astronautics. https://doi.org/10.2514/6.2006-6662.

Hill, K.A., Born, G.H., 2008. Autonomous Orbit Determination from Lunar Halo Orbits Using Crosslink Range. J. Spacecraft Rock. 45 (3), 548–553. https://doi.org/10.2514/1.32316.

Imken, T., Sherwood, B., Elliott, J., Frick, A., McCoy, K., Oh, D., Kahn, P., Karapetian, A., Polit-Casillas, R., Cable, M., 2016. Sylph-a SmallSat probe concept engineered to answer Europa's big question. In: AIAA/USU Conference on Small Satellites, pp. 1–10. https://digitalcommons.usu.edu/smallsat/2016/TS11SciPayload1/6/.

Iraci, G., Gnam, C., 2018. An Open Source Radio for Low Cost Small Satellite Ranging. In: AIAA/USU Conference on Small Satellites, pp. 1–8. https://digitalcommons.usu.edu/smallsat/2018/all2018/399/.

Krener, A.J., Ide, K., 2009. Measures of unobservability. In: Proceedings of the 48h IEEE Conference on Decision and Control (CDC) held jointly with 2009 28th Chinese Control Conference, pp. 6401–6406. IEEE. https://doi.org/10.1109/cdc.2009.5400067.

Leonard, J., Jones, B., Villalba, E., Born, G., 2012. Absolute Orbit Determination and Gravity Field Recovery for 433 Eros Using Satellite-to-Satellite Tracking. In: AIAA/AAS Astrodynamics Specialist Conference. American Institute of Aeronautics and Astronautics. https://doi.org/10.2514/6.2012-4877.

Leonard, J.M., 2015. Supporting Crewed Missions using LiAISON Navigation in the Earth-Moon System. University of Colorado, Ph. D. thesis.

Lou, T., Fu, H., Zhang, Y., Wang, Z., 2015. Consider unobservable uncertain parameters using radio beacon navigation during Mars entry. Adv. Space Res. 55 (4), 1038–1050. https://doi.org/10.1016/j.asr.2014.11.016.

Meng, F., Wu, X., Ou, G., 2010. Autonomous orbit determination of navigation constellation based on inter-satellite ranging and ranging rate. J. Spacecraft TT&C Technol. 29 (4), 89–94.

Mercer, C., 2018. Planetary Science Deep Space SmallSat Studies. In Lunar Planetary Science Conference Special Session. The Woodlands, Texas. https://www.nasa.gov/sites/default/files/atoms/files/00_psds3_overview.pdf.

Mercer, C.R., 2019. Small Satellite Missions for Planetary Science. In: AIAA/USU Conference on Small Satellites. Utah State University, Logan, UT, pp. 1–6.

Montenbruck, O., Gill, E., 2000. Satellite Orbits. Springer, Berlin, Heidelberg. https://doi.org/10.1007/978-3-642-58351-3.

NASA, 2015. Artemis 1 Secondary Payloads, AES EM-1 Secondaries Fact Sheet. URL https://www.nasa.gov/sites/default/files/atoms/files/aes-secondaries-fs-v508c.pdf (accessed June 2020).

NASA, 2020. What is CAPSTONE? URL https://www.nasa.gov/directorates/spacetech/small_spacecraft/capstone (accessed Aug 2020).

Qin, T., Qiao, D., Macdonald, M., 2019. Relative Orbit Determination Using Only Intersatellite Range Measurements. J. Guidance Control Dyn. 42 (3), 703–710. https://doi.org/10.2514/1.g003819.

Rebordão, J.M., 2013. Space optical navigation techniques: an overview. In: SPIE Proceedings, vol. 8785, pp. 29–48. https://doi.org/10.1117/12.2026063.

Rowe, S., Kruzelecky, R., Murzionak, P., Sinclair, I., Corriveau, M., Walker, R., Vennekens, J., Gao, Y., Bridges, C., Baresi, N., Lucca Fabris, A., Cloutis, E., St-Amour, A., Silva, N., Gameiro, M., 2021. Lunar Volatile and Mineralogy Mapping Orbiter (VMMO): Viable Science from Lunar CubeSats. In: AIAA/USU Conference on Small Satellites. Utah State University, Logan, UT, pp. 1–10.

Scotti, M., Botteron, C., Rico, M., Basile, F., Massaras, V., Kieniewicz, B., Svaton, J., Giordano, P., Ventura-Traveset, J., 2022. NaviMoon - Ultra-High Sensitivity GNSS Receiver for Lunar Navigation. In: NAVITEC 2022, pp. 7–7.

Sheikh, S.I., Pines, D.J., Ray, P.S., Wood, K.S., Lovellette, M.N., Wolff, M.T., 2006. Spacecraft navigation using X-ray pulsars. J. Guidance Control Dyn. 29 (1), 49–63. https://doi.org/10.2514/1.13331.

Speretta, S., Turan, E., Cervone, A., Menicucci, A., Topputo, F., Franzese, V., Giordano, C., Merisio, G., Lizia, P.D., Massari, M., Labate, D., Taiti, A., Pilato, G., Bertels, E., Paskeviciute, A., Woroniak, K., Koschny, D., Vennekens, J., Walker, R., 2022.

LUMIO: A CubeSat to Monitor Micro-meteoid Impacts on the Lunar Farside. In: 2022 IEEE Aerospace Conference (AERO). IEEE, pp. 1–8. https://doi.org/10.1109/aero53065.2022.9843311.

Tanis, T.P., 2022. Autonomous Orbit Determination in Cislunar Space. Delft University of Technology, Delft, the Netherlands, Master's thesis.

Tapley, B., Schutz, B.E., Born, G.H., 2004. Statistical Orbit Determination. Elsevier Academic Press, Burlington, USA. https://doi.org/10.1016/B978-0-12-683630-1.X5019-X.

Thelen, A.E., Chanover, N., Murphy, J., Rankin, K., Stochaj, S., 2017. A Europa CubeSat concept study for measuring atmospheric density and heavy ion flux. J. Small Satellit. 6, 591–607.

Thompson, M.R., Forsman, A., Chikine, S., Peters, B.C., Ely, T., Sorensen, D., Parker, J., Cheetham, B., 2022. Cislunar Navigation Technology Demonstrations on the CAPSTONE Mission. In: The International Technical Meeting of the The Institute of Navigation, Long Beach, California, pp. 471–484. https://doi.org/10.33012/2022.18208.

Turan, E., Speretta, S., Gill, E., 2022a. Autonomous crosslink radionavigation for a Lunar CubeSat mission. Front. Space Technol. 3, 1–12. https://doi.org/10.3389/frspt.2022.919311.

Turan, E., Speretta, S., Gill, E., 2022b. Autonomous navigation for deep space small satellites: Scientific and technological advances. Acta Astronaut. 193, 56–74. https://doi.org/10.1016/j.actaastro.2021.12.030.

Turan, E., Speretta, S., Gill, E., 2022c. Autonomous Navigation Performance of Cislunar Orbits considering High Crosslink Measurement Errors. In: 2022 IEEE Aerospace Conference (AERO). IEEE, pp. 1–11. https://doi.org/10.1109/aero53065.2022.9843772.

Walker, R., Binns, D., Bramanti, C., Casasco, M., Concari, P., Izzo, D., Feili, D., Fernandez, P., Fernandez, J.G., Hager, P., Koschny, D., Pesquita, V., Wallace, N., Carnelli, I., Khan, M., Scoubeau, M., Taubert, D., 2018. Deep-space CubeSats: thinking inside the box. Astron. Geophys. 59 (5), 524–530. https://doi.org/10.1093/astrogeo/aty232.

Wang, W., Shu, L., Liu, J., Gao, Y., 2019. Joint navigation performance of distant retrograde orbits and cislunar orbits via LiAISON considering dynamic and clock model errors. Navigation 66 (4), 781–802. https://doi.org/10.1002/navi.340.

Woo, S., Gao, J., Mills, D., 2010. Space network time distribution and synchronization protocol development for mars proximity link. In: SpaceOps 2010 Conference. American Institute of Aeronautics and Astronautics, pp. 1–13. https://doi.org/10.2514/6.2010-2360.

Yim, J., Crassidis, J., Junkins, J., 2000. Autonomous orbit navigation of interplanetary spacecraft. In: Astrodynamics Specialist Conference. American Institute of Aeronautics and Astronautics, pp. 1–9. https://doi.org/10.2514/6.2000-3936.